
Article:
Freeman, F. orcid.org/0000-0002-7402-1790, Chechik, L. orcid.org/0000-0002-7626-2694, Thomas, B. et al. (1 more author) (2023) Calibrated closed-loop control to reduce the effect of geometry on mechanical behaviour in directed energy deposition. Journal of Materials Processing Technology, 311. 117823. ISSN 0924-0136

https://doi.org/10.1016/j.jmatprotec.2022.117823

Journal of Materials Processing Tech. 311 (2023) 117823

Contents lists available at ScienceDirect

Journal of Materials Processing Tech.

journal homepage: www.elsevier.com/locate/jmatprotec

Calibrated closed-loop control to reduce the effect of geometry on mechanical behaviour in directed energy deposition

F. Freeman [a,*], L. Chechik [a], B. Thomas [a], I. Todd [a]

[a] Department of Materials Science and Engineering, The University of Sheffield, Mappin Street, S1 3JD, UK

ARTICLE INFO

Associate Editor: Marion Merklein

Keywords:
Directed energy deposition
Closed loop control
Melt pool monitoring
Mechanical properties
Additive manufacturing

ABSTRACT

Directed energy deposition (DED) is an emerging technology with significant industrial potential in the repair of critical aerospace components, however its adoption has been limited by concerns about geometry-driven microstructural and mechanical property variation. These could be resolved by controlling the local temperature field, which would result in a consistent and predictable cooling profile. Closed-loop control approaches have been investigated previously, but with limited assessment of mechanical properties and only on small builds. In this work, we confirm that using fixed build parameters results in a statistically significant, geometry-driven variation in the bulk mechanical properties of DED-built 316 L steel. To address this issue, we have developed an industrially-suitable control algorithm using a low-cost coaxial camera, applying statistical process control techniques to identify representative melt pool images from the livestream. This has been tested on long builds, maintaining a control adjustment frequency of 1 Hz on build durations of > 1 h. Performance has been quantified through bulk mechanical testing, which confirmed that the control algorithm successfully eliminated the component-scale trends in melt pool size, and achieved a geometry-agnostic process with improved mechanical homogeneity.

1. Introduction

Metal additive manufacturing (AM) technologies have been rapidly moving into the mainstream (Shrinivas Mahale et al., 2022), adopted by industries from healthcare to aerospace (DebRoy et al., 2018), and with particular importance for high-value, low-volume manufacturing. One of the key metal AM processes, directed energy deposition (DED) uses a powder stream, fed into the focal point of a laser beam, to deposit a molten track and build up a 3D component (Thompson et al., 2015). DED has a high degree of geometric flexibility, suitable both for manufacture and repair, but the adoption of DED for safety-critical components has been limited by challenges related to homogeneity, structural integrity, and variability of mechanical performance (Blakey-Milner et al., 2021).

These issues could be mitigated by reducing variation in the local temperature field, which in turn would yield a more controllable solidification rate, cooling profile and in-situ reheating (Yadollahi et al., 2015), enabling predictable microstructures and mechanical properties. Mirazimzadeh et al. (2022) modelled a range of DED scan strategies for different component geometries and reported that scan strategy and component geometry both influence the stress field in the built component, due to differences in the temperature field during solidification and cooling. While Hofman et al. (2012) showed that component geometry affected bead width, substrate dilution and hardness in laser cladding, a very similar technology to DED.

Akbari and Kovacevic (2019) monitored the deposition of a single-walled 316 L steel sample with coaxial imaging, and observed that the baseplate acted as a heat sink, pulling heat out of the melt pool and causing it to shrink, resulting in the base of the sample being thinner than the top. Earlier work by Bi (2006a), had reported a similar effect on single-walled 316 L steel samples, and also showed corresponding trends in microstructure and hardness. A further development by Chechik et al. (2020) used side-view imaging to monitor DED of thin walled samples (6 hatches, 2.7 mm thickness), and found cooling rate to be higher close to the baseplate, as expected from a smaller melt pool. This raises the possibility that different machine set-ups and clamping strategies could change the strength of this heat sink and cause differences in the manufactured product.

At the component scale, Gibson et al. (2020), investigated a range of control algorithms on wire-feed DED of Ti-6Al-4V, and reported that

* Corresponding author.
E-mail address: f.freeman@sheffield.ac.uk (F. Freeman).

https://doi.org/10.1016/j.jmatprotec.2022.117823
Received 1 August 2022; Received in revised form 10 November 2022; Accepted 13 November 2022
Available online 17 November 2022

fixed build parameters resulted in poor dimensional control at the trailing edge of aerofoil-style geometries. This was due to oversize melt tracks caused by depositing directly adjacent to the previous hatch before the heat from that hatch had dissipated. This local geometry effect is a common issue across additive manufacturing platforms, with Craeghs et al. (2011) publishing findings from laser powder-bed fusion (LPBF) showing the local temperature field to be affected by overhangs and exposed corners, and Catchpole-Smith et al. (2017) using fractal area-filling scan strategies to achieve a more uniform temperature profile and reduce cracking in LPBF-built nickel superalloys.

Closed-loop control approaches show good potential as a route to achieving a predictable and controllable DED product. These take a signal from a live process monitoring sensor, extract characteristics that describe the current build behaviour, and adjust the build parameters to achieve and maintain a target characteristic. A number of studies exist in the literature, but no strong consensus has yet been reached on one particular approach (Tapia and Elwany, 2014).

A photodiode monitoring approach, such as that used for control in DED (Bi et al., 2006a) and in laser cladding (Bi et al., 2006b), provides the simplest signal by generating a single value based on the overall intensity of the field of view. This is often referred to as the temperature, although calibration to a physical temperature requires an understanding of the effect of emissivity, which itself is a function of temperature, surface oxidation, material and wavelength (Zhang et al., 2015).

Camera-based monitoring provides much more information about the melt pool than photodiodes, including the shape and distribution of intensity across the image. Hofman et al. (2012) used an optical camera (400–1000 nm wavelength, 200 Hz) to monitor a laser cladding process, while for monitoring DED, Akbari and Kovacevic (2019) used a near-infrared camera (700+ nm wavelength, 200 Hz) and Farshidianfar et al. (2021) used a thermal infrared camera (7.5–14 μm wavelength, 30 Hz).

One potential drawback to camera-based approaches is that they generate large volumes of data very quickly. When considering a DED process with travel speeds in excess of 1000 mm/min, it is necessary to balance the required frequency of control adjustments with the ability to collect, transfer, process and store data. Additionally, the high frame-rate cameras used in the literature can be prohibitively expensive outside a research environment.

A number of studies using camera-based control have also found it necessary to incorporate image processing techniques (filtering, smoothing, fitting) prior to extracting the required measurement from the image. Akbari and Kovacevic (2019) binarised the image using a fixed threshold and applied a fast Fourier transform. They attributed abrupt, high frequency variations in the transformed data to spatter, and excluded this with a low-pass filter before applying the inverse transform to achieve a noise-reduced image. They then applied a circle-fitting technique to identify the location of the melt pool, and extracted the width. Su et al. (2022) similarly used filtering to remove noise from melt pool images before extracting the width as a control input. Hofman et al. (2012) used a single-step process, applying a Gauss-shaped point spread function to remove single bright pixels which they attributed to spatter, before measuring melt pool width. However, image-processing increases the calculation time and neither study discusses how successfully the spatter is removed from the image, or whether the image-processing has influenced the subsequent measurement.

Analysis of melt pool images from additive manufacturing processes can also be carried out for the identification of build defects as they occur. The literature on this has often concentrated on complex techniques including the neural networks and deep learning approaches used by Kwon et al. (2020) and Yang et al. (2019). An alternative approach, developed by Liao et al. (2022), used a finite-element simulation combined with live monitoring of melt pool depth for DED power modulation. For industrial applications, these have a high barrier to entry, requiring complex coding, significant computing power and large volumes of training data.

Camera-based systems provide a wider scope for extracting descriptive characteristics. A widely-used technique is to determine a threshold intensity value corresponding to the edge of the melt pool, and from this measure either a width (Akbari and Kovacevic, 2019) or an area (Hu et al., 2002). Using the width allows the virtual measurement to be calibrated to a physical measurement from a built component, as demonstrated by Akbari and Kovacevic (2019), adding a link in the chain of process qualification. Melt pool images have also been used with pixel tracking to calculate live cooling rates (Farshidianfar et al., 2021).

The next stage is the adjustment of the control parameter, based on this input. DED has a large number of build parameters including power, speed, hatch spacing, layer thickness, scan strategy and powder flow rate. Commonly, the adjusted parameter is either the laser power (Akbari and Kovacevic, 2019) or travel speed (Farshidianfar et al., 2021), but studies have also considered live modifications to the scan strategy to avoid localised heat build-up (Nassar et al., 2015). Comprehensive parameter studies have demonstrated that laser power is the most significant factor affecting melt pool width (Qi et al., 2010). Additionally, by controlling on laser power, the distance travelled between control points is uniform across the component.

While there are many studies investigating different ways to incorporate closed-loop control within DED, there is limited evidence for it improving bulk mechanical properties. As Smoqi et al. (2022) identifies, the majority of DED closed-loop control studies produce comparatively small samples, often only single-hatch walls, not representative of a production-size components. From an industrial perspective, knowing that a control algorithm is sufficiently robust to operate without issues over a representative build duration is extremely useful, particularly when it relies on transferring large volumes of data between different components of a control system. Further, while these studies demonstrate improved stability in the measured characteristic (e.g. melt pool width), this only confirms that the control algorithm is affecting that characteristic, not necessarily that it is improving the built product.

Farshidianfar et al. (2021) used dendrite arm spacing and hardness to analyse their control approach, but the data would benefit from further statistical analysis as the results are not conclusive. Smoqi et al. (2022) showed that closed-loop control yielded a more uniform porosity distribution and greater microstructural homogeneity at the grain-size scale, but the effect on microhardness and cooling rate (determined from dendrite arm spacing) was less clear. Akbari and Kovacevic (2019) also stated their control approach yielded a more uniform solidification cell size, although the difference in projected cooling rate was minimal. Hofman et al. (2012) showed a clearer effect from closed-loop control in laser cladding, measuring hardness as a function of depth for a deposition with varying substrate thickness. A very recent work by Su et al. (2022) reports tensile data, but the test samples were cut from single hatch walls, with the gauge section including only 1–2 layers and taking three samples from each build condition, which is insufficient for analysing statistical significance.

In this work, we have concentrated on developing a closed-loop control approach that could be easily applied to an industrial process and validating its effect on bulk mechanical properties. To achieve this, we have incorporated a low-cost coaxial camera, running at a comparatively low frame rate, within an industrial-scale DED system. We have used statistical filtering methods to identify representative images from the live-stream as the control input, rather than filtering and smoothing the individual images. Using simple single-walled geometries, we have calibrated the greyscale intensity to identify the melt pool edge, generate a width measurement and used this to control laser power. We have then tested this approach across a range of single walled and block geometries, and demonstrated that it delivers a reduction in geometry-driven mechanical property variation.

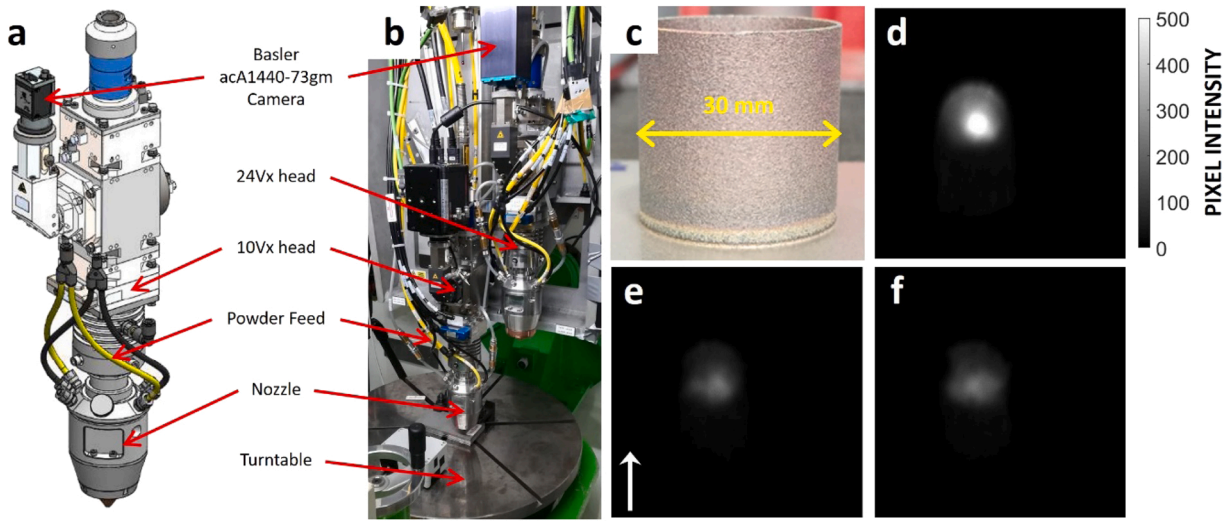

Fig. 1. a) Schematic of the 10Vx DED head used in this work, showing the location of the coaxial Basler camera, the powder feed pipework and the nozzle; b) Image of the DED build chamber, also showing the 24Vx head (not used in this work) and the turntable; c) Cylinder built at 250 W, 2200 mm/min, repeat #1 showing good build quality with uniform surface finish; d) Coaxial image from cylinder built at 350 W, 2200 mm/min showing high intensity melt pool; e) Coaxial image from cylinder built at 250 W, 2200 mm/min repeat #1 showing lower intensity melt pool; f) Coaxial image from cylinder built at 250 W, 2200 mm/min repeat #2 showing comparable melt pool intensity to repeat #1. Melt pool images show the 0–500 section of the intensity range for ease of viewing; all analysis used the full 0–4095 range.

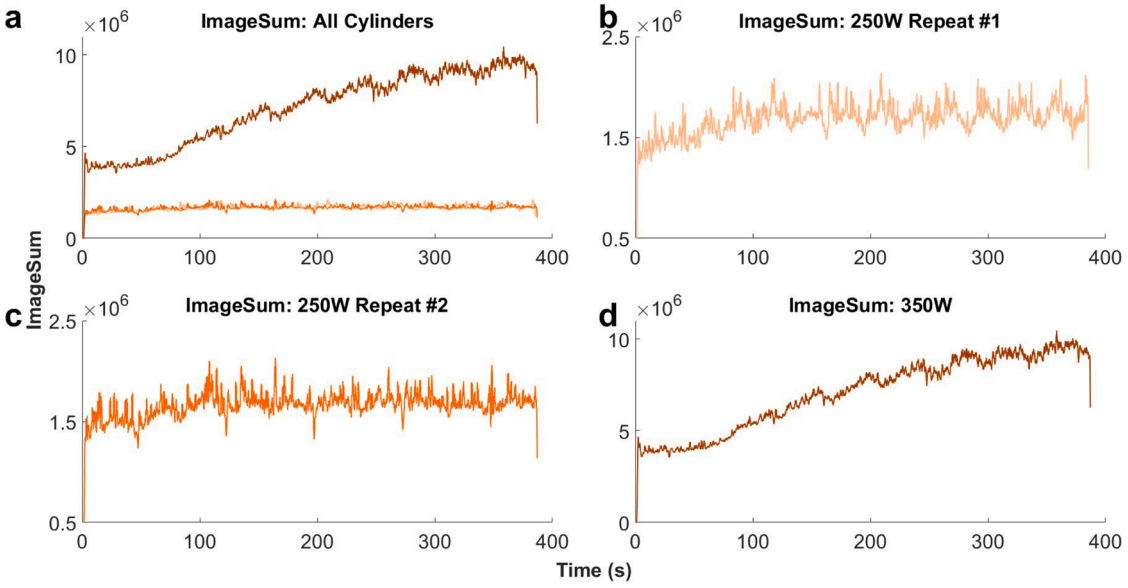

Fig. 2. ImageSum for GA316 cylinders as a moving average over 30 images (≈1 s); a) All three cylinders combined; b) Cylinder at 250 W 2200 mm/min Repeat #1; c) Cylinder at 250 W 2200 mm/min Repeat #2; d) Cylinder at 350 W 2200 mm/min. Scale of b) and c) is expanded compared to that in a) and d) for clarity.

2. Experimental

The powder used was gas atomised 316 L steel powder from Sandvik (referred to here as GA316), at a flow rate of 7.2 ± 1.3 g/min (Freeman et al., 2021). The powder had a nominal size range of 45–90 μm.

Builds were carried out on a 5-axis BeAM Magic 800 Directed Energy Deposition system, with a 0.75 mm laser spot diameter (10Vx build head) and a 3.5 mm working distance (Fig. 1a-b). Imaging was carried out using a co-axial Basler acA1440–73gm camera with CMOS sensor, filtered to accept wavelengths in the range 660 – 1000 nm, excluding reflected light from the laser. 12-bit images, with 500 × 500 pixel field of view, were collected from the camera at 28 frames per second with an exposure of 4000 μs. The 12-bit range extends from 0 to 4095 for each pixel, but the majority of images only required the 0–500 section of this range; adjusting to a longer exposure time would use more of the range.

All build parameters quoted are the nominal values used in the program, without adjustment for any efficiency losses through the optics.

Builds without control included helical cylinders and blocks. The cylinders were built by moving the nozzle slowly in the vertical linear axis (Z) and rotating the turntable around the horizontal C axis, while keeping the horizontal linear axes (X & Y) and tilt axis (B) fixed. The cylinders were 30 mm diameter and 30 mm tall, built using 250 W and 350 W laser power, at a travel speed of 2200 mm/min and a 0.2 mm layer height. The cylinder at 250 W power was repeated to analyse the process variation.

The blocks used 270 W power, 2200 mm/min travel speed, 50 mm hatch length, 0.2 mm layer thickness and 0.4 mm hatch spacing. The

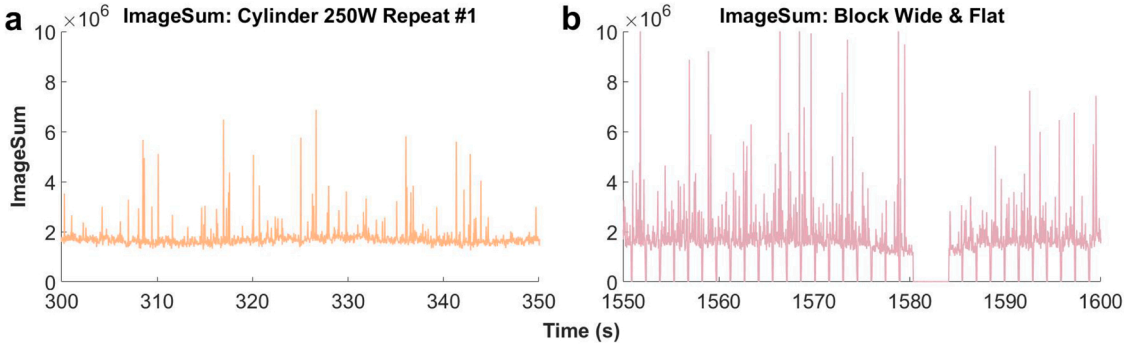

Fig. 3. ImageSum for every image from a) GA316 cylinder at 250 W 2200 mm/min Repeat #1; b) GA316 Wide & Flat block with 80 hatches and 25 layers at 270 W 2200 mm/min. Block data shows short drops in ImageSum every 1.4 s, corresponding to the end of each hatch, and longer drops corresponding to the end of each layer.

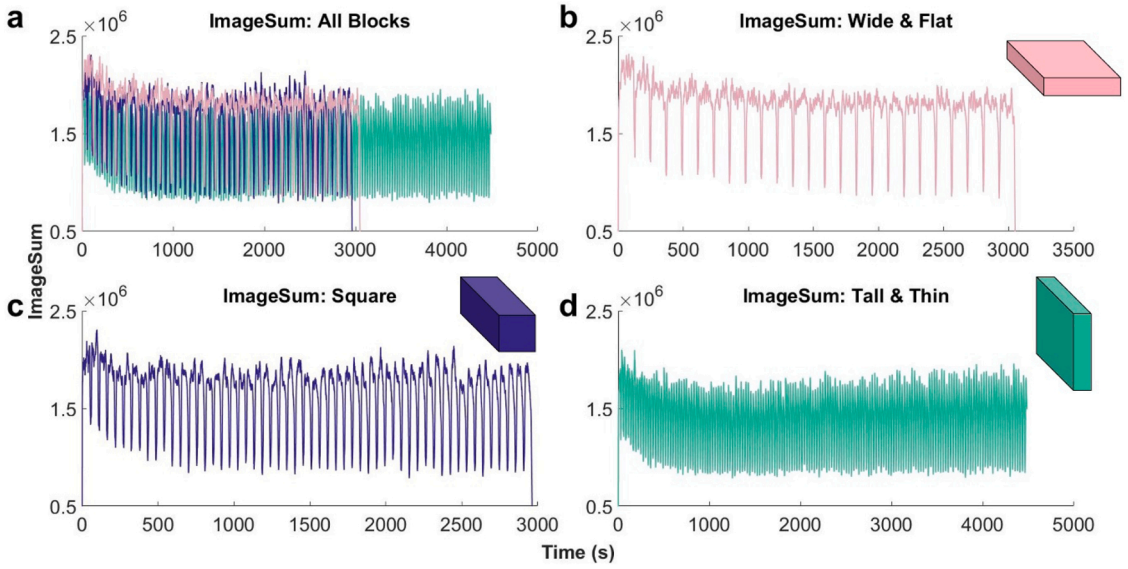

Fig. 4. ImageSum for GA316 blocks as a moving average over 300 images (≈10 s), all built at 270 W 2200 mm/min; a) All three blocks combined; b) Wide & Flat block with 80 hatches and 25 layers; c) Square section block with 34 hatches and 55 layers; d) Tall & Thin block with 16 hatches and 165 layers. Periodic drops in ImageSum correspond to the laser switching off between layers.

'Wide & Flat' block had 80 hatches and 25 layers (32 ×5×50 mm); the 'Square' block had 34 hatches and 55 layers (13.6 ×11×50 mm), while the 'Tall & Thin' block had 16 hatches and 165 layers (6.4 ×33×50 mm). All blocks used a raster pattern, with hatches deposited in alternating direction across each layer.

Identical blocks were built with control, using the same build files but allowing power to be determined by the control algorithm. In addition, a set of cylinders were built with control, all 30 mm high, at 0.2 mm layer height, but with different diameters and travel speeds. The smallest cylinder was 10 mm diameter, with a travel speed of 1400 mm/min and starting power of 250 W. The medium cylinder was 20 mm diameter with a travel speed of 1800 mm/min and a starting power of 300 W. The largest cylinder was 30 mm diameter with a travel speed of 2200 mm/min and a starting power of 300 W.

Test pieces were harvested from the block samples for 3-point bend testing (span 28.2 mm). The nominal test-piece size was 45 × 3×3 mm, with the actual dimensions of each individual test-piece measured before bending. The load-displacement was converted to flexural stress-strain, and the maximum stress achieved was determined for each test-piece individually.

3. Results & discussion

3.1. Baseline without control

The single-walled cylinders all showed good build quality, with smooth sides and no visible defects (Fig. 1c). Fig. 1d-f shows the 2000th image from each of the cylinder builds. The 12-bit images can achieve an intensity range of 0–4095; Fig. 1d-f show just the 0–500 section of this range to allow the melt pool to be observed more easily. Videos from the start and middle of each build are also available in the Appendix. The top of each image is the leading edge of the melt pool and the right side of each image is the outer face of the cylinder.

The coaxial images captured from the cylinders were initially analysed using 'ImageSum', defined as the sum of the intensity of all the pixels in the image. With 12-bit images (0–4095) containing 500 × 500 pixels, ImageSum can range from 0 to 10^9.

The time series of ImageSum with build height, displayed as a moving average over 30 images (≈1 s), showed a gradual increase as the build progressed upwards from the baseplate (Fig. 2). The 350 W build had a higher ImageSum throughout, with a more significant increase than the 250 W builds and was still increasing at the end of the build. The two 250 W builds showed comparable behaviour, with any difference between them being negligible compared to the difference between

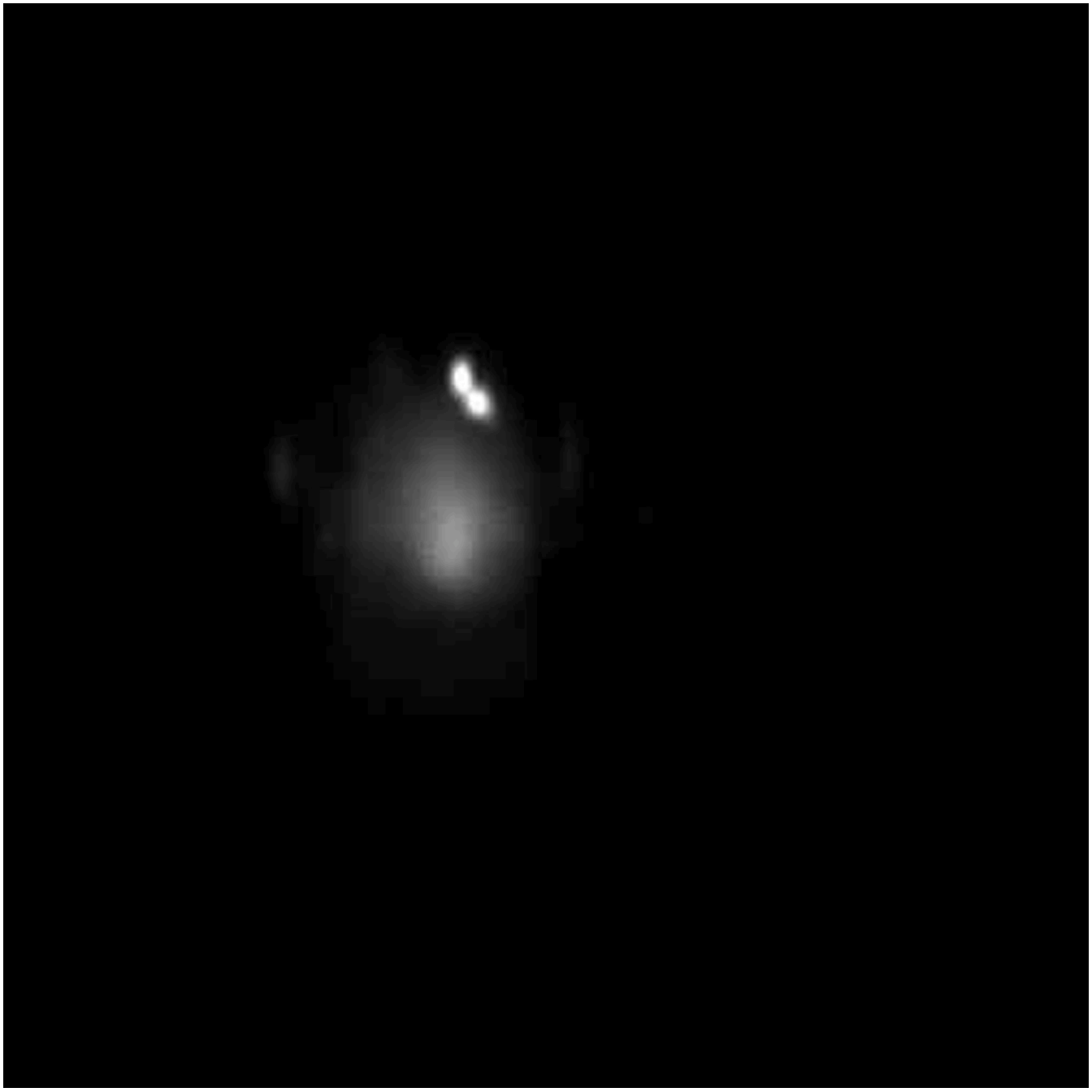

Video 1. A video clip is available online. Supplementary material related to this article can be found online at doi:10.1016/j.jmatprotec.2022.117823.

the 250 W and 350 W builds.

The effect of build geometry on ImageSum was further explored with three blocks of different cross sections. False-colour videos of the coaxial monitoring of the blocks are available in the Appendix, covering 300 images (≈10 s of build time, 7–8 hatches) showing the position of the melt pool within the image shifting depending on travel direction.

The data from the blocks was much noisier than that of the cylinders, possibly due to the laser changing direction and switching off between layers and hatches. This is illustrated in Fig. 3, which shows the ImageSum for every image (not a moving average) in a 50 s window from Repeat #1 of the 250 W cylinders and from the 'Wide & Flat' block.

The data for the 'Wide & Flat' block (80 hatches, 25 layers) showed that ImageSum dropped every 1.4 s, for 2–3 images, before increasing again. These drops appeared in groups of 80 repetitions, separated by 25 longer drops lasting around 100 images. Examination of the data on nozzle position and laser power confirmed that these drops coincided with the ends of hatches and layers, and corresponding patterns were observed in the data for the other two blocks.

For the blocks, the time series of ImageSum with build height (Fig. 4) is displayed as a moving average over 300 images (≈10 s); a longer window than used for the cylinders to counteract the increased noise.

The blocks showed a gradual decrease in ImageSum at the start of the build, in contrast to the increase observed with the cylinders. There was also a drop in ImageSum at the end of each layer, when the laser switched off and the nozzle moved back to the start position. For the 'Tall & Thin' block, with only 16 hatches per layer, this noise was very

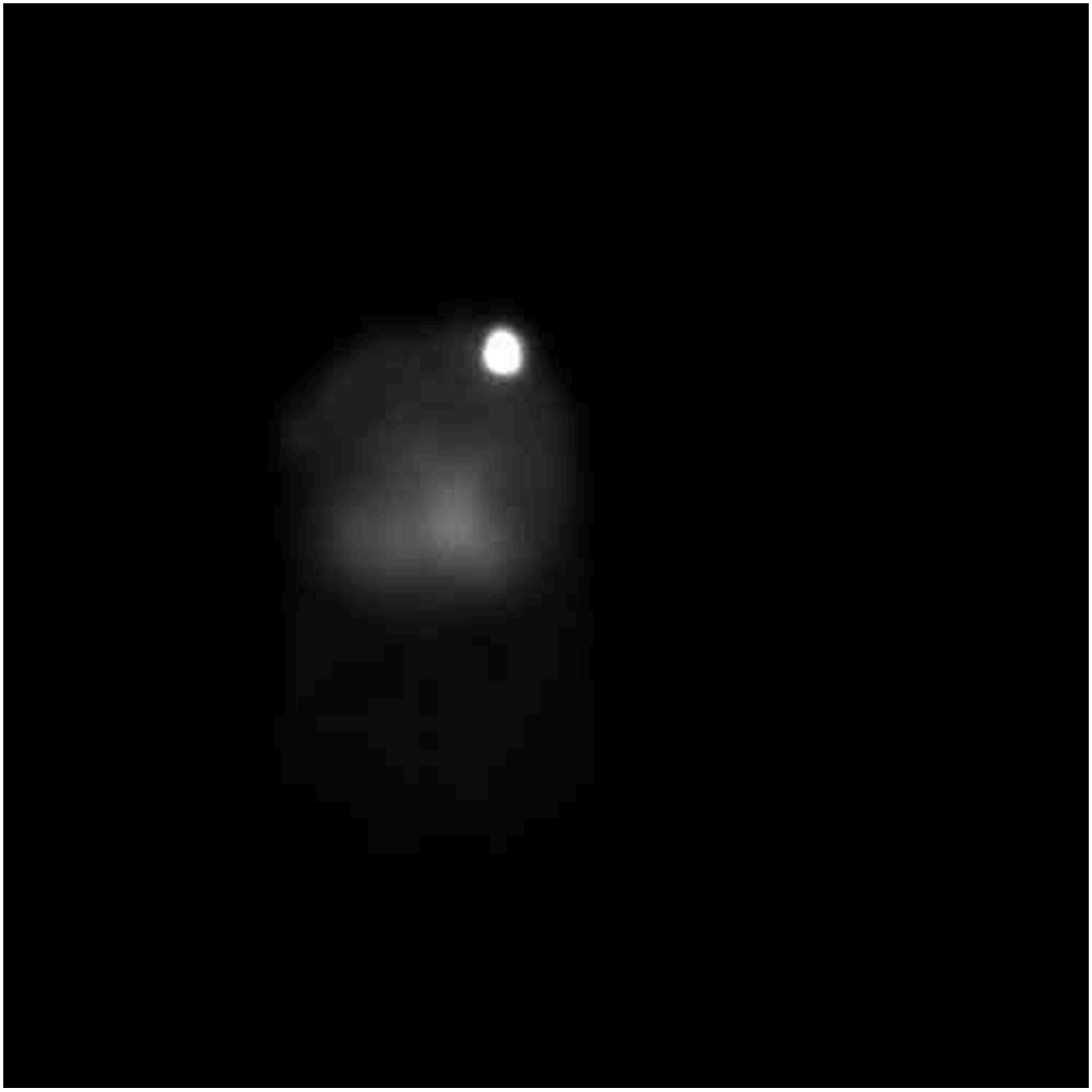

Video 2. A video clip is available online. Supplementary material related to this article can be found online at doi:10.1016/j.jmatprotec.2022.117823.

significant.

A final observation was that all builds showed frequent incidences of very high ImageSum values ($> 3 \times 10^6$), most clearly seen in Fig. 3. It was identified that these were from images with small, very intense regions, probably caused by the ejection of hot particles from the melt pool (spatter). This can be observed in the videos 1–13 (Appendix).

ImageSum provides useful information about the build behaviour, but it is a relatively coarse parameter, given that a small, hot melt pool could generate an image with the same ImageSum as a larger, cooler melt pool. This has been investigated using data from the Repeat #1 of the 250 W, 2200 mm/s cylinder (Fig. 5).

Image #932, near the start of the build, had an ImageSum of 1.686×10^6 and shows a small, bright melt pool with spatter at the leading edge. Image #8191, near the end of the build, had an ImageSum of 1.697×10^6, and shows a larger, lower intensity melt pool. While the exact ImageSum values are slightly different, they were both close to the mean ImageSum for the whole build (1.683×10^6) and the difference between them was only 2% of the standard deviation (5.009×10^5), so they are judged to have a sufficiently comparable ImageSum for this assessment.

3.2. Control algorithm design

3.2.1. Noise filtering

As shown above and in the videos (Appendix), the livestream of raw image data was noisy, including images where the laser was off and images with spatter, and therefore required filtering. The aim of the filtering was not to select the best image at a given time, or perfectly

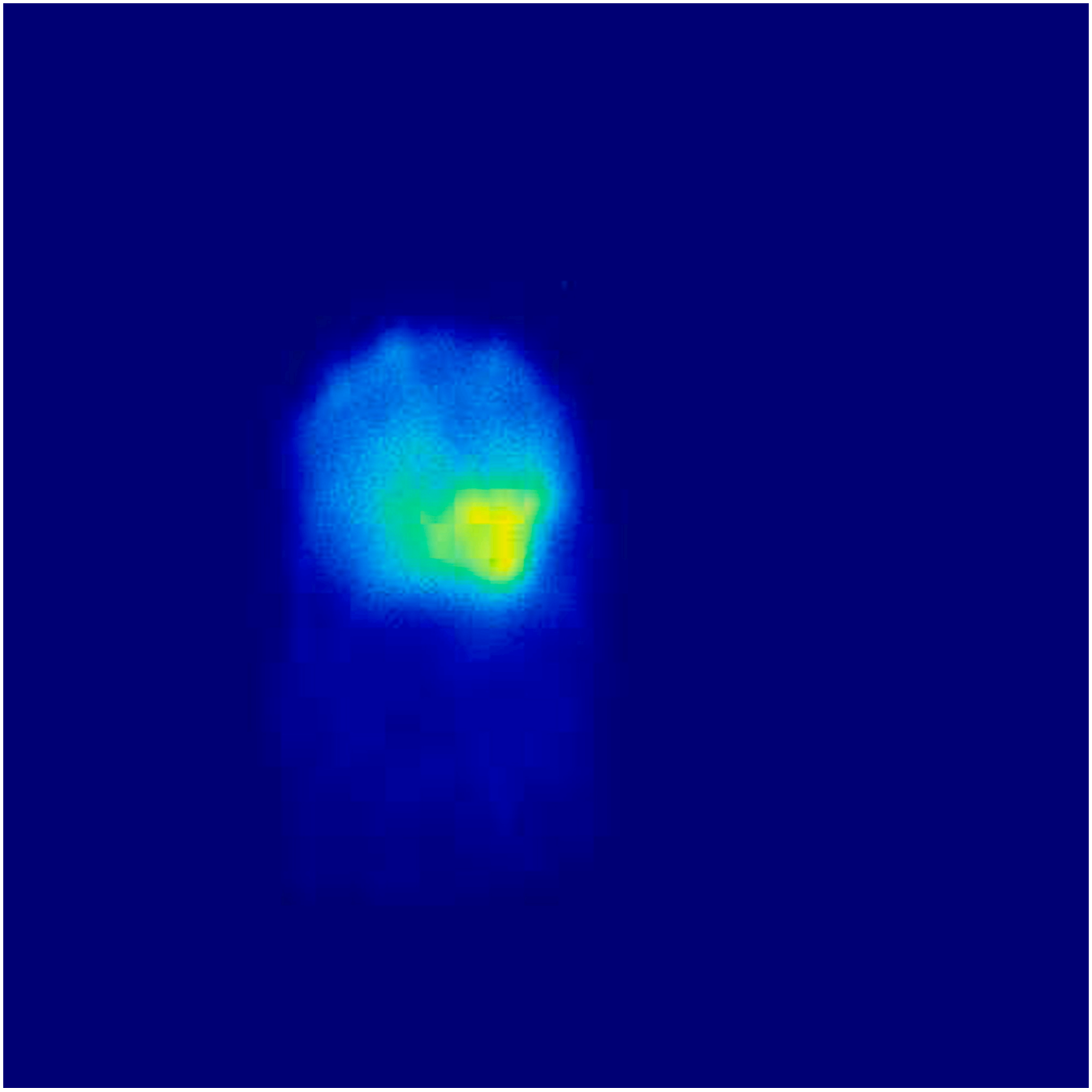

Video 3. A video clip is available online. Supplementary material related to this article can be found online at doi:10.1016/j.jmatprotec.2022.117823.

identify those with spatter, but to give a computationally efficient way to ensure the images used for the control input were representative of the current melt pool condition. The behaviour of the filtering sequence is illustrated in Fig. 6, using a set of images from the Square block build.

A control loop was triggered every 30 images, capturing approximately 1 s of build time and the ImageSum was calculated for each image individually (Fig. 6a). This number of images was selected as it is commonly regarded as the minimum number of observations for statistical analysis. A higher number would reduce the update frequency, while a smaller number would potentially reduce the ability to eliminate non-representative images.

The first stage was to remove images where there was no melt pool, as these were considered to be a separate population from those required for the control input. Histograms of the ImageSum data for each block (Fig. 7) showed split distributions; the majority of the ImageSum data in the range 1×10^6 to 5×10^6 but with a second peak below 1.5×10^5, corresponding to the images at the ends hatches and layers. It was judged that a fixed threshold of 1.5×105 would be an efficient way to exclude the majority of the dark images, retaining only those judged to contain a visible melt pool (Fig. 6b).

The next stage was to ensure the images used for width measurement were representative of the current melt pool condition. The remaining image set was used to calculate the ImageSum mean, $\bar{x}$, and standard deviation, σ, and to define thresholds at $(\bar{x}+\sigma)$ and $(\bar{x}-\sigma)$. Those with ImageSum outside the $\pm1\sigma$ thresholds were filtered out (Fig. 6c), an approach based on statistical process control techniques (Stapenhurst, 2005, pp. 14–16). The calculations of mean and standard deviation were quick, allowing them to be updated for each control loop based on the

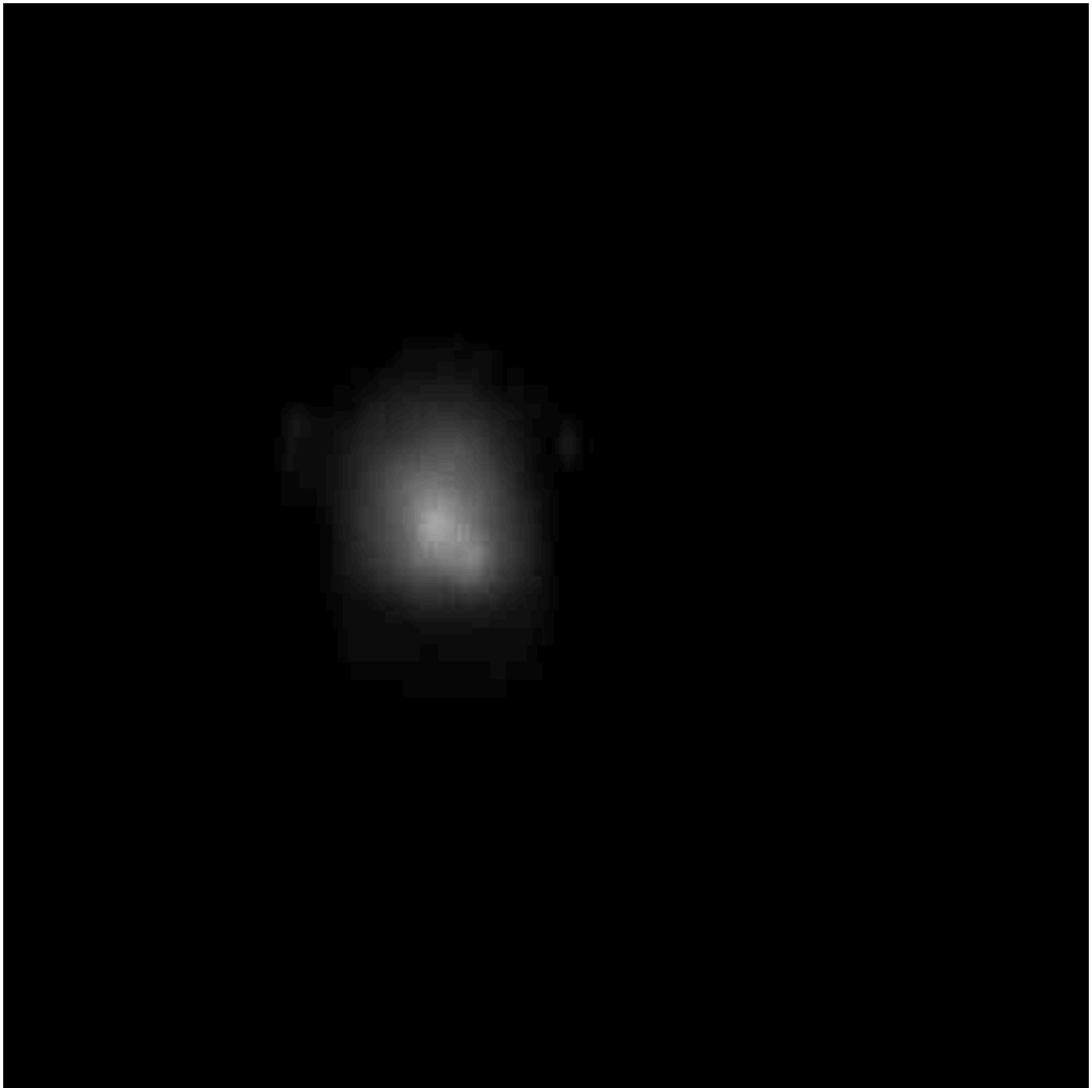

Video 4. A video clip is available online. Supplementary material related to this article can be found online at doi:10.1016/j.jmatprotec.2022.117823.

current image set.

Updating the mean and standard deviation on each control loop ensured that the filtering range responded to underlying trends in the ImageSum data and differences between components, such as the baseplate heat sink effect discussed earlier.

Finally, from the set of images which passed the filtering, the most recent 5 were used as the control input (Fig. 6d) as these are most representative of the current state of the process. If, at any stage, there were fewer than 5 images to pass to the next stage, the loop terminated and restarted with a new set of images.

In the example illustrated in Fig. 6, four images were filtered out for being outside the filtering thresholds; these are shown in the top row of Fig. 8 and all exhibit 'hotspots' associated with spatter. Five images were selected for width measurement; these are shown in the bottom row of Fig. 8, and all have clear melt pools with no apparent spatter.

This approach was computationally efficient, as calculating ImageSum and applying the filtering thresholds were comparatively quick calculations. Extracting melt pool width, which was used as the control input was more computationally intensive, but was only carried out on images which had passed the filtering process and were judged to be representative of the current melt pool condition. In an offline test, calculation of the filtering thresholds took 2 ms for the full set of 30 images, while width measurement took 1 ms per image, giving an overall time of 7 ms per loop with the filtering approach, a 4x reduction against $>$ 30 ms if width was measured on every image. This becomes more important during a build, when the computer is also managing the livestream from the camera and communication with the BeAM over the OPC-UA interface.

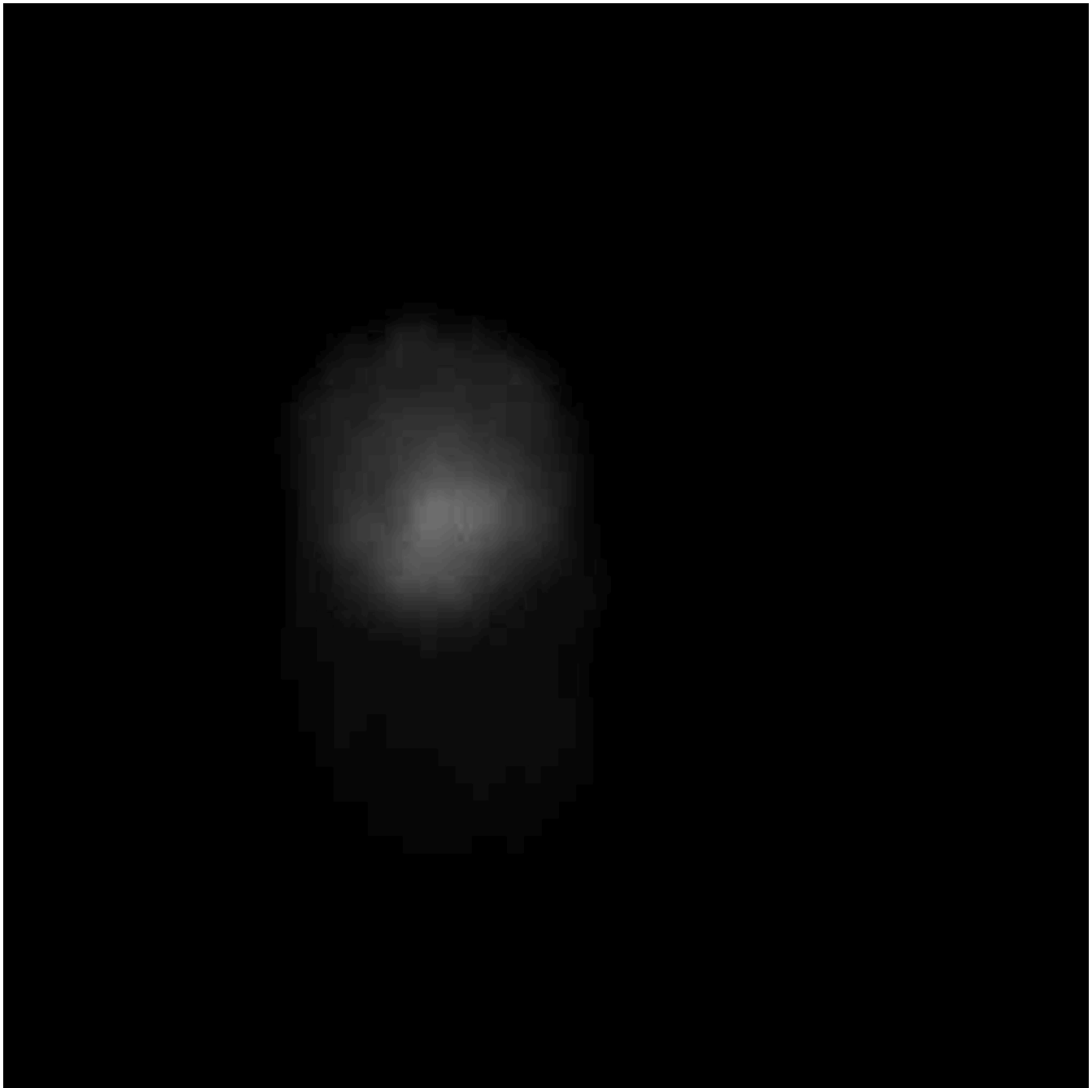

Video 5. A video clip is available online. Supplementary material related to this article can be found online at doi:10.1016/j.jmatprotec.2022.117823.

3.2.2. Calibration

To use the images as the input to a closed-loop control algorithm, the melt pool width was measured, where the greyscale threshold defining the melt pool edge was calibrated against physical measurements from a single-walled build (Akbari and Kovacevic, 2019).

The physical measurements were taken from the single-walled cylinders, which were built keeping the nozzle stationary and rotating the turntable around the vertical axis. This fixed the position of the melt pool within the image, keeping melt pool width parallel to the horizontal axis of the image (Fig. 1).

To determine the greyscale threshold for the GA316 powders, the cylinders were sectioned vertically with a cutting wheel and the width of the single hatch wall was measured using calipers at 5 positions from base to top, with 3 measurements at each position. Caliper measurements were taken slightly back from the cut surface to avoid the effect of flash at the cut edge.

Measuring at multiple heights accommodated the increase in width observed during the build (Fig. 9a). The images were analysed, varying the greyscale threshold to minimise the error between the image width and the physical width over all positions on all cylinders (Fig. 9b). The minimum error was achieved by defining the melt pool edge at a greyscale value of 18.

The width measurement was extracted from the image by binarising using the greyscale threshold, and extracting a bounding box across the resulting black & white image (Fig. 9c-e).

The coaxial images collected from the earlier GA316 cylinders and blocks were post-processed through the control algorithm described above to generate a width time series. The cylinders (Fig. 10a) showed

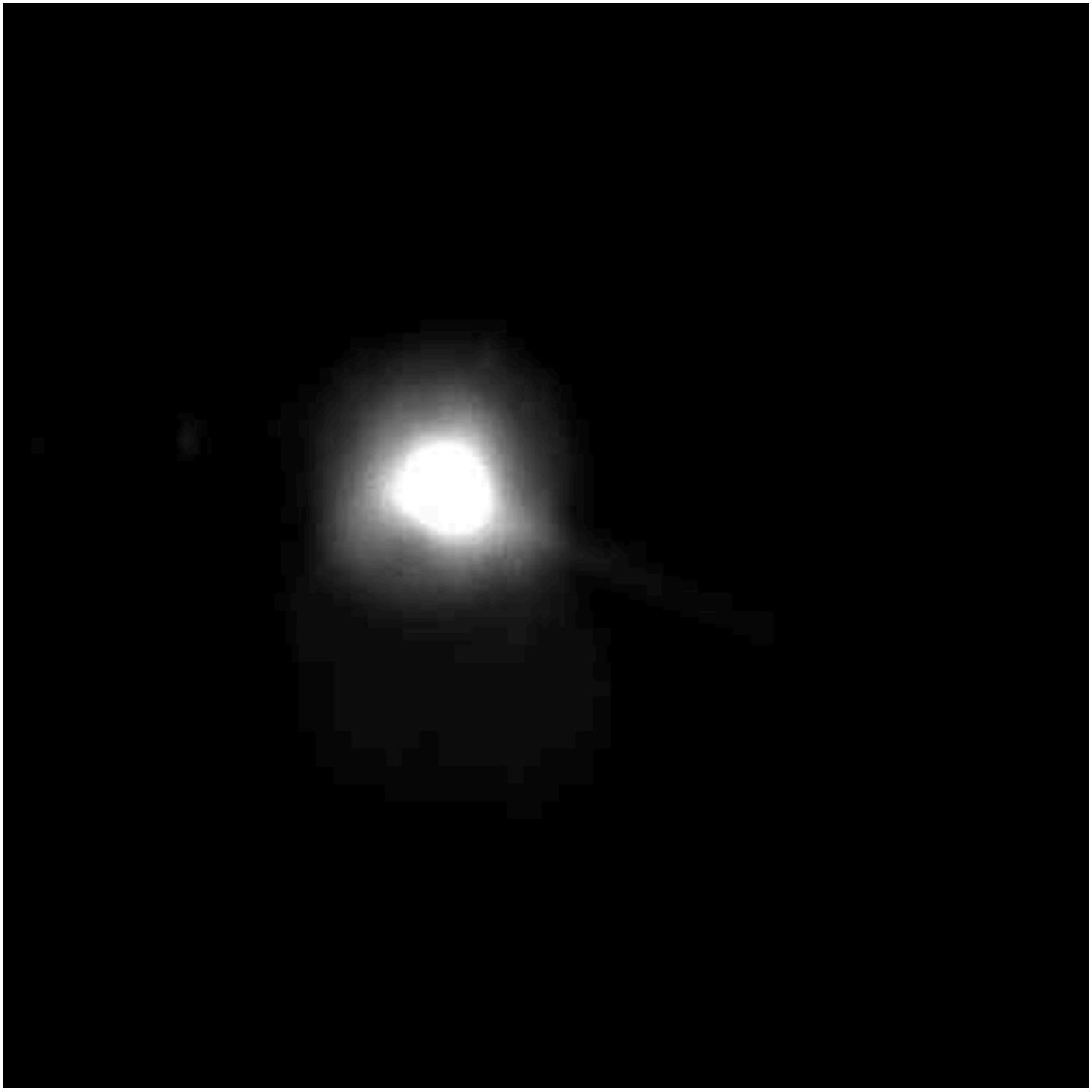

Video 6. A video clip is available online. Supplementary material related to this article can be found online at doi:10.1016/j.jmatprotec.2022.117823.

an increase in width at the start of the build, as expected from the literature.

The blocks (Fig. 10b-d) all showed a decrease in width over the first 1000 s of the build, at varying levels and in contrast to the increase observed with the cylinders. This was least apparent in the Square block, but the melt pool width of the Tall & Thin block reduced by 80 μm during the first 500 s of build time (20 layers, 4 mm build height). This has not been reported previously, and highlights the extent to which geometry influences the balance between different heat loss mechanisms.

The data from the blocks was extremely noisy, with limited stabilisation. Analysing the data for the second half of each build only, to exclude the baseplate heat sink effect, there was evidence of a component geometry effect, with a statistically significant difference in the median width between the three geometries (Kruskal-Wallis test, $p = 0.000$); the Wide&Flat block achieved a width of 829 ± 62 μm, the Square block achieved a width of 815 ± 65 μm, while the Tall&Thin block achieved a width of 776 ± 58 μm.

3.2.3. Power modulation

The second part of the control algorithm was the adjustment of laser power. The measured width was divided by the target width to give an error ratio ϵ (e.g. measured 880 μm, target 800 μm, error ratio 1.1). The error ratio ϵ was converted to a scaling factor F using the following relationship, where the value of β determined the strength of power adjustment. To prevent damage to the machine, F was limited to a maximum of 1.5 and minimum of 0.5.

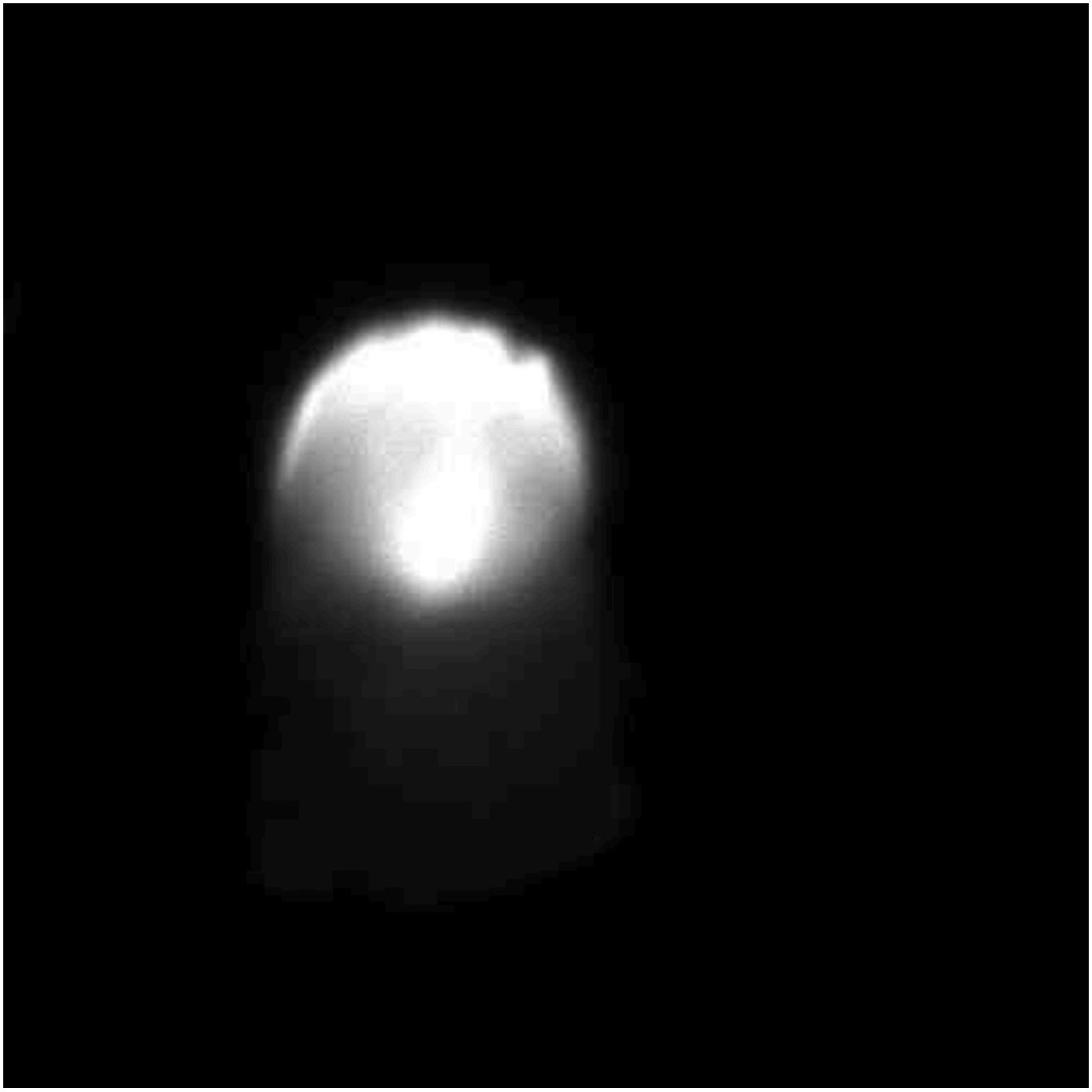

Video 7. A video clip is available online. Supplementary material related to this article can be found online at doi:10.1016/j.jmatprotec.2022.117823.

$$F = \beta(1-\epsilon)+1$$

The scaling factor was pushed to the BeAM through the OPC-UA interface, and applied to the initial power set in the programme G-code. A programme with an initial power of 300 W, with a scaling factor of 0.8 therefore produced an instantaneous power of 240 W.

A series of blocks, 6 hatches wide and 20 layers high, were used to assess the performance of different values of β, with the aim of correcting deviations quickly without causing oscillation through over-correction; good results were achieved with $\beta = 0.50$. The calculation used at this stage was relatively simple, compared with the techniques in the literature, and a more complex calculation could be applied in future if required.

The resolution of the power modulation is determined by the resolution of the original image, the target width and the current power. In these images, 1 pixel = 5.4 μm, giving a scaling factor resolution of 0.00338 for a target width of 800 μm. For a current power of 270 W, this corresponds to a power modulation step size of 0.911 W. A larger step size would be driven by a lower image resolution, a smaller target width or a larger initial power.

3.3. Validation

The control algorithm was tested by building a series of simple geometries: blocks (as previously) and cylinders with different diameters and initial laser power/speed. The blocks were direct repeats of those previously built without control, using the same program, while the cylinders at 20 mm and 10 mm diameter were new geometries which

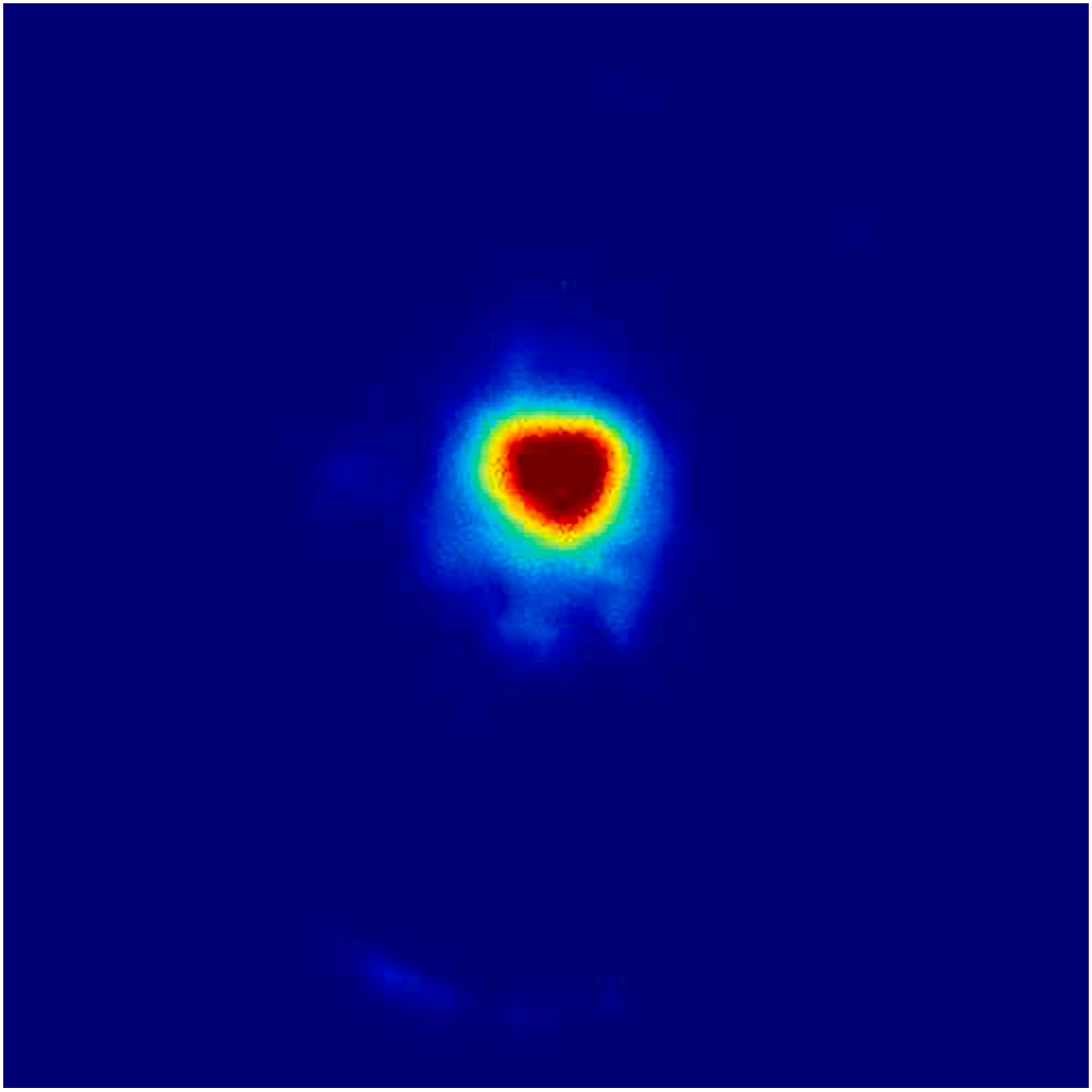

Video 8. A video clip is available online. Supplementary material related to this article can be found online at doi:10.1016/j.jmatprotec.2022.117823.

were only built using control.

As the cylinder diameter reduces, the time for the laser to return over a given position also reduces, giving less time for heat to dissipate away. If the laser power is not reduced, or the travel speed increased, sufficiently to counteract effect this then there is a risk of the melt pool size increasing to the extent that it may bridge to the nozzle, causing the build to fail and potentially damaging the nozzle. Given this risk, there was no attempt to build the smaller cylinders using the same starting conditions without control.

The 30 mm diameter cylinder was built first, with an initial power of 300 W based on an average of the earlier 'No Control' cylinder builds. The 20 mm diameter cylinder was then built, reading across the starting power of 300 W; this stabilised to a final power of 212 W, a scaling factor of 0.7. As the control algorithm limits to a scaling factor between 0.5 and 1.5 of the initial power, the initial power for the 10 mm cylinder was set to 250 W, expecting that it would require an even lower final power. The cylinder speeds were chosen to avoid excessive rotational speed which could damage the turntable, given that these were built with the nozzle stationary and the turntable rotating around the vertical axis.

The builds all converged on the target width of 800 μm within 20 s (Fig. 11 & Table 1), and maintained this throughout the build duration. For the Square block, the mean interval between control adjustments was 1.04 ± 0.30 s with a standard deviation of 0.30 s, correlating well with the programmed frequency. There were no errors or lags in image capture from the camera, or in data transfer across the OPC-UA interface between the control algorithm and the BeAM equipment.

At a fixed travel speed of 2200 mm/min, this control frequency

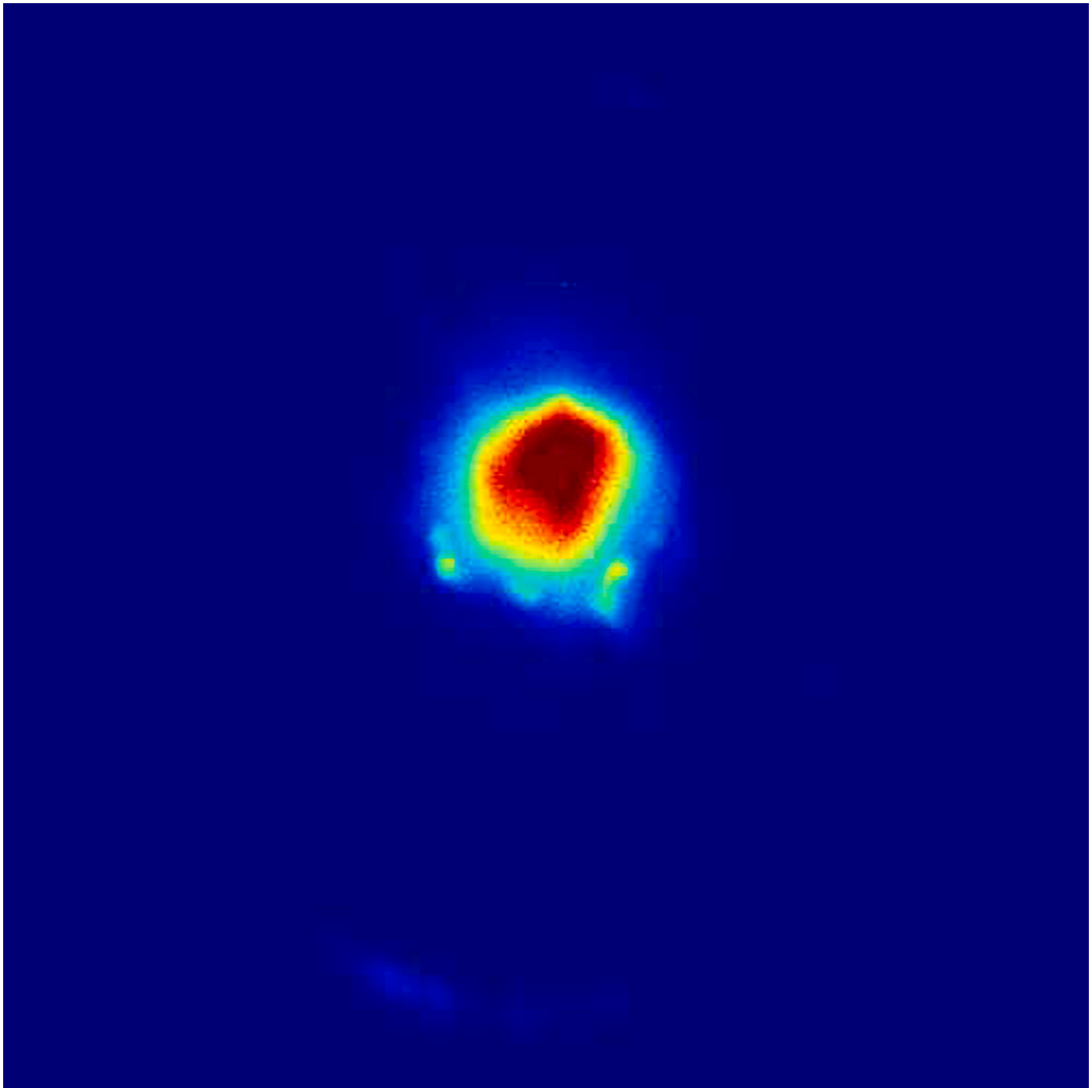

Video 9. A video clip is available online. Supplementary material related to this article can be found online at doi:10.1016/j.jmatprotec.2022.117823.

corresponds to one control point every 36 mm. This gave good results for a component with a hatch length of 50 mm, but might not be appropriate for components with smaller features. In this situation, the control loop could be triggered from fewer images, allowing a higher control frequency.

The blocks without control had displayed an initial drop in width during the first 1000 s of the build; this was successfully corrected in the control builds, which showed a stable width measurement during this time and a corresponding increase in power (Fig. 12). While the control algorithm corrected for component-scale trends, it did not affect the low-level noise which was comparable with and without control (Table 1).

The blocks manufactured from GA316 with and without control were stress relieved using a heat treatment (650 °C for 2 h) and then sectioned by EDM into matchsticks, each approximately 45 × 3×3 mm for 3-point bend testing. The tests were used to generate flexural stress-strain curves and extract the ultimate flexural strength (Fig. 12). Bend test samples were only harvested from the blocks, the single wall cylinders were too thin and curved for meaningful data to be collected.

Bend testing was selected as it permitted a large number of samples to be harvested from the blocks, yielding 35 samples from each of the 'No Control' and 'With Control' conditions, and a minimum of 11 samples from each individual geometry, enabling meaningful statistical analysis. This also allowed an assessment of the spread of mechanical properties throughout each block. Bend testing is more forgiving of internal porosity, which can be an issue with additively manufactured parts, but it was regarded as appropriate for this study assessing the impact of component geometry and control on the variation in

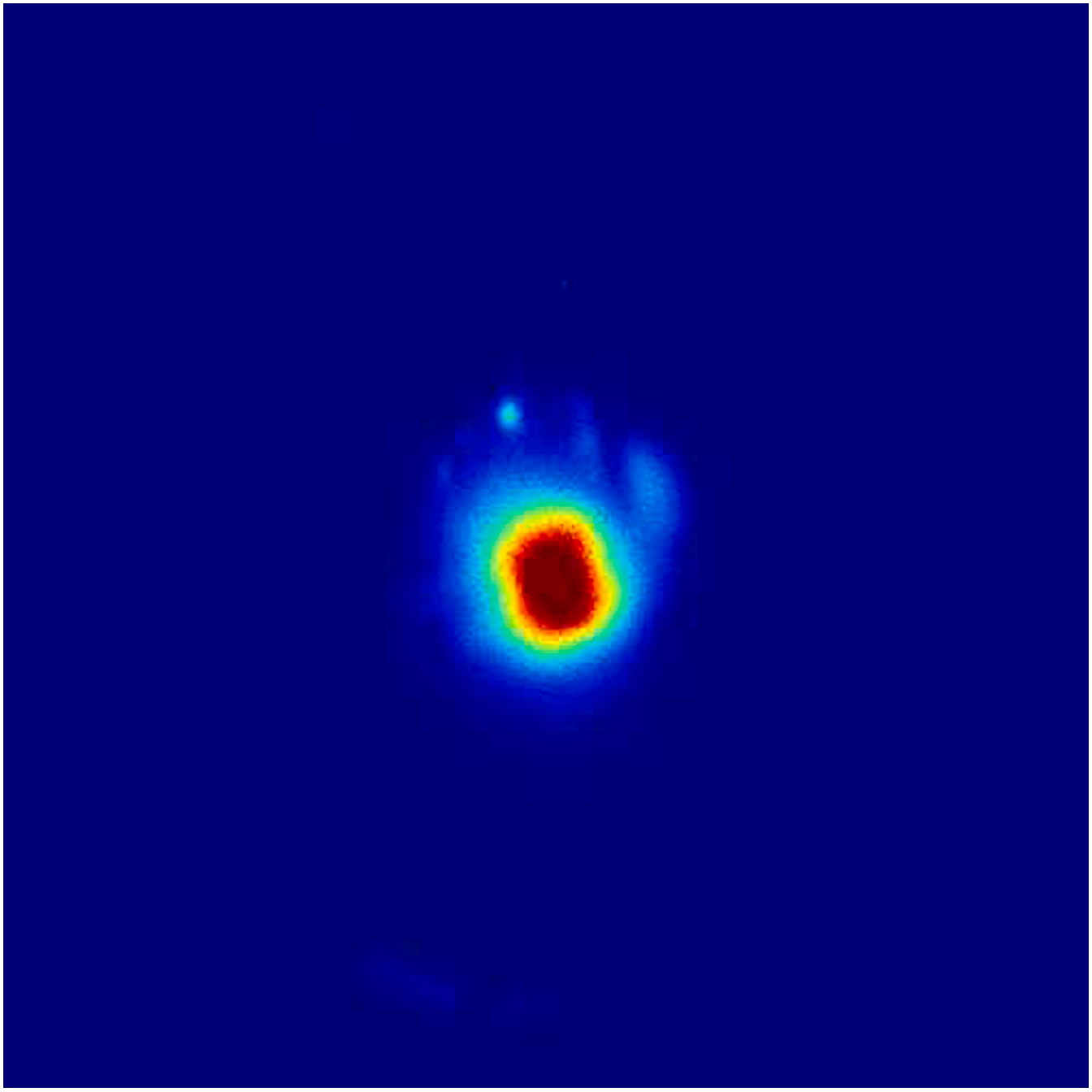

Video 10. A video clip is available online. Supplementary material related to this article can be found online at doi:10.1016/j.jmatprotec.2022.117823.

mechanical properties (Fig. 13).

The ultimate flexural strength (UFS) was used to compare the two control conditions by applying a series of statistical tests in Minitab. The first analysis compared the UFS distribution for 'No Control' and 'With Control' overall, with UFS data from all three block geometries combined (Fig. 12c-d):

1. The data for 'No Control' and 'With Control' each fitted a normal distribution (Anderson-Darling test, $p > 0.1$ in both cases).
2. The mean of the 'No Control' and 'With Control' datasets were not significantly different (2-sample T-test, $p = 0.365$).
3. The variance of the 'With Control' dataset was smaller than that of the 'No Control' dataset (2-Variances test, $p = 0.004$).
4. The Weibull modulus of the 'With Control' dataset (36.9) was higher than that of the 'No Control' dataset (22.5).

The second analysis considered the UFS distribution from the three block geometries individually (Fig. 12e-f):

1. The data from each block geometry individually fitted a normal distribution (Anderson-Darling test, $p > 0.1$ in all cases).
2. The means for the 'No Control' blocks were different (1-way ANOVA, $p = 0.011$).
3. The means for the 'With Control' blocks were not different (1-way ANOVA, $p = 0.250$).

Using control has achieved more consistent mechanical behaviour,

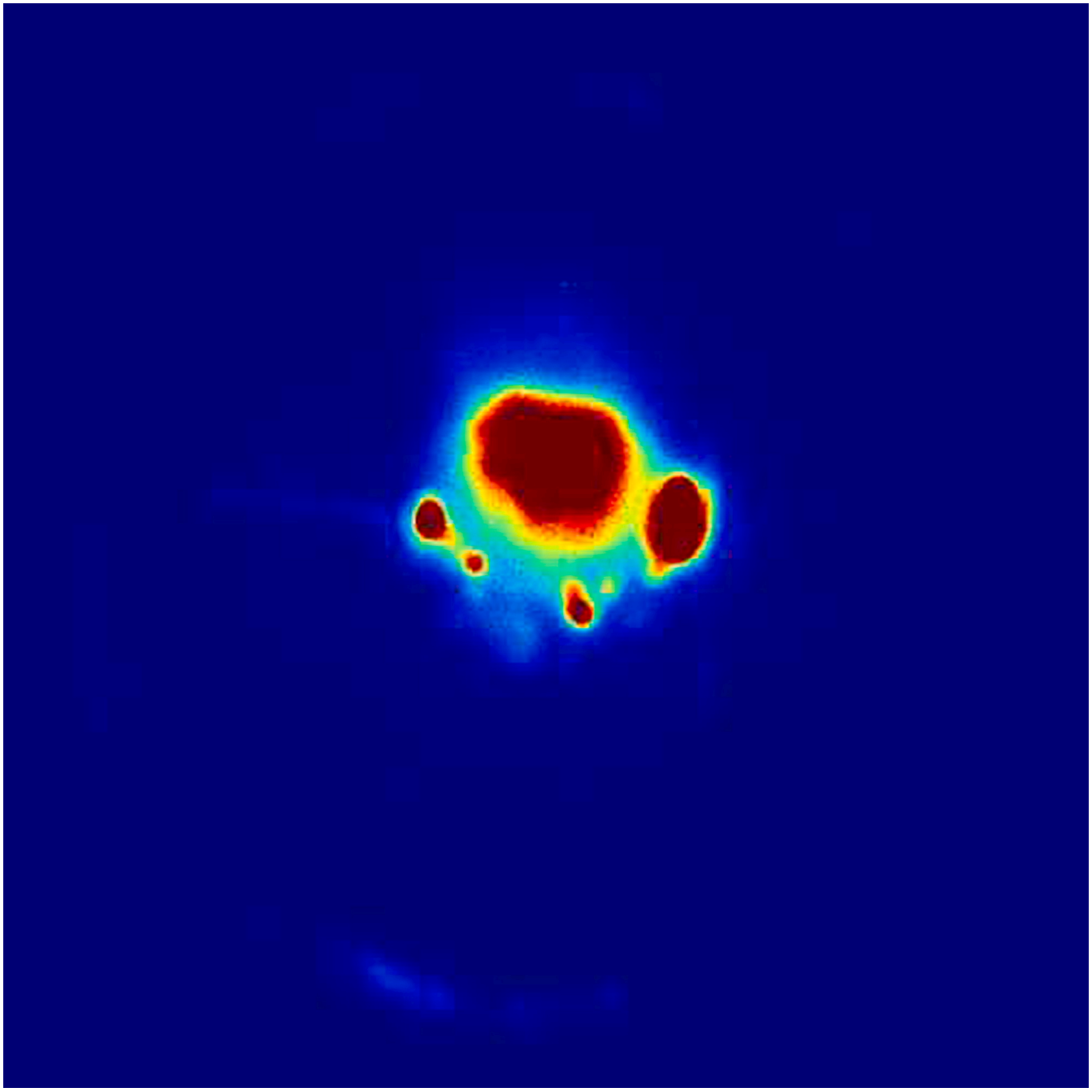

Video 11. A video clip is available online. Supplementary material related to this article can be found online at doi:10.1016/j.jmatprotec.2022.117823.

which was the goal of this work. Reducing variation is an essential first step in process improvement, creating a solid baseline for subsequent activity. Once the variation (noise) is minimised, it is easier to assess whether changes to the input conditions (e.g. target width) have carried through to an improvement in mechanical properties.

4. Summary & conclusions

The aim of this work was to develop a simple image-based closed-loop control system for DED, and use it to investigate the effect of component geometry on mechanical properties. This incorporated a low-cost coaxial camera running at a comparatively low frame rate on an industrial-scale DED system, using statistical filtering to identify representative images for the control input. The control system was tested across a range of geometries, including larger components with long build times to confirm robustness, and validated by statistical analysis of mechanical test data.

The statistical filtering approach was designed to provide a computationally efficient method of ensuring the control input consisted only of images known to be typical of the current melt pool condition. It was not designed to be perfect at identifying images with spatter, or those where the laser was off. Further, it was judged to be faster and more robust than running noise reduction on each image individually.

Statistical process control is commonly used to monitor the output of conventional manufacturing processes, and is therefore well understood by industry. Other studies have used fast Fourier transforms (Akbari and Kovacevic, 2019) or noise filtering (Hofman et al., 2012) to remove spatter from the individual images, but these risk affecting the

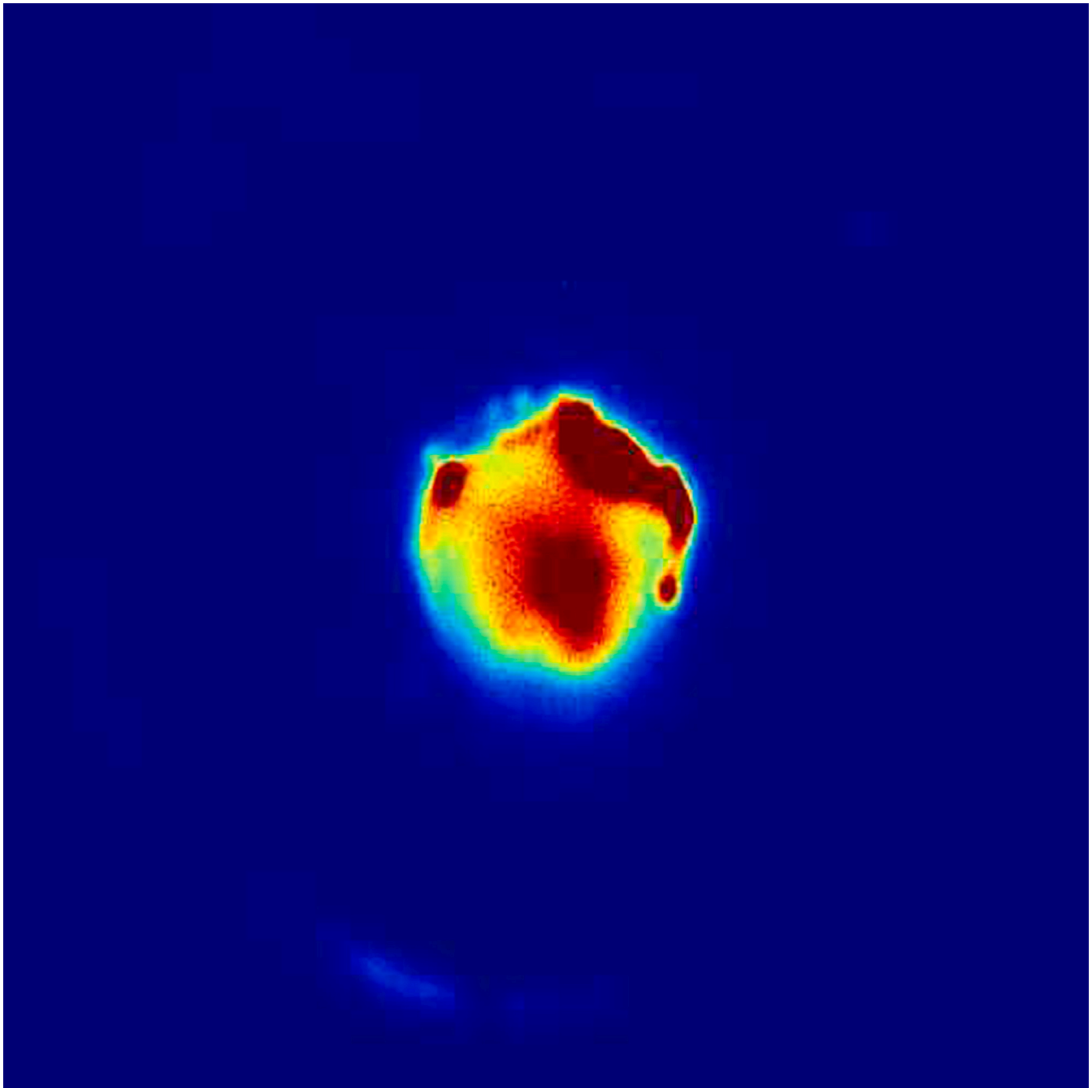

Video 12. A video clip is available online. Supplementary material related to this article can be found online at doi:10.1016/j.jmatprotec.2022.117823.

subsequent measurement. The statistical process control approach takes measurements from the unmodified images, which produces a more traceable result, and avoids the computing burden of more complex techniques.

Melt pool width was selected as the control parameter, being straightforward to measure both on the physical component and on the images, and has been used successfully in the literature (Akbari and Kovacevic, 2019). False colour videos from the cylinders show a long tail at the bottom of the image (opposite to travel direction), which could be the trailing edge of the melt pool or could be a stream of hot gas, both of which would contribute to the intensity of the image in this region. As the camera cannot distinguish between these, the measurement of melt pool length and area are judged to be less reliable than the measurement of width.

Single walled cylinders built without control showed an increase in melt pool width with build height; this has been reported previously and attributed to the heat sink effect of the baseplate. However, the multi-hatch blocks built without control showed the opposite, with melt pool width decreasing during the early layers, highlighting how geometry influences the competing heat loss mechanisms.

The mechanical properties of the blocks were quantified by 3-point bend tests using samples harvested from the blocks. This showed that the variance of the ultimate flexural strength distribution 'With Control' was tighter than that from 'No Control' and the Weibull modulus 'With Control' was higher than 'No Control'. The Weibull modulus is a parameter which maps the probability of failure; a higher modulus denotes a more homogenous material with more predictable behaviour.

Further, the analysis showed that the means of the three 'No Control'

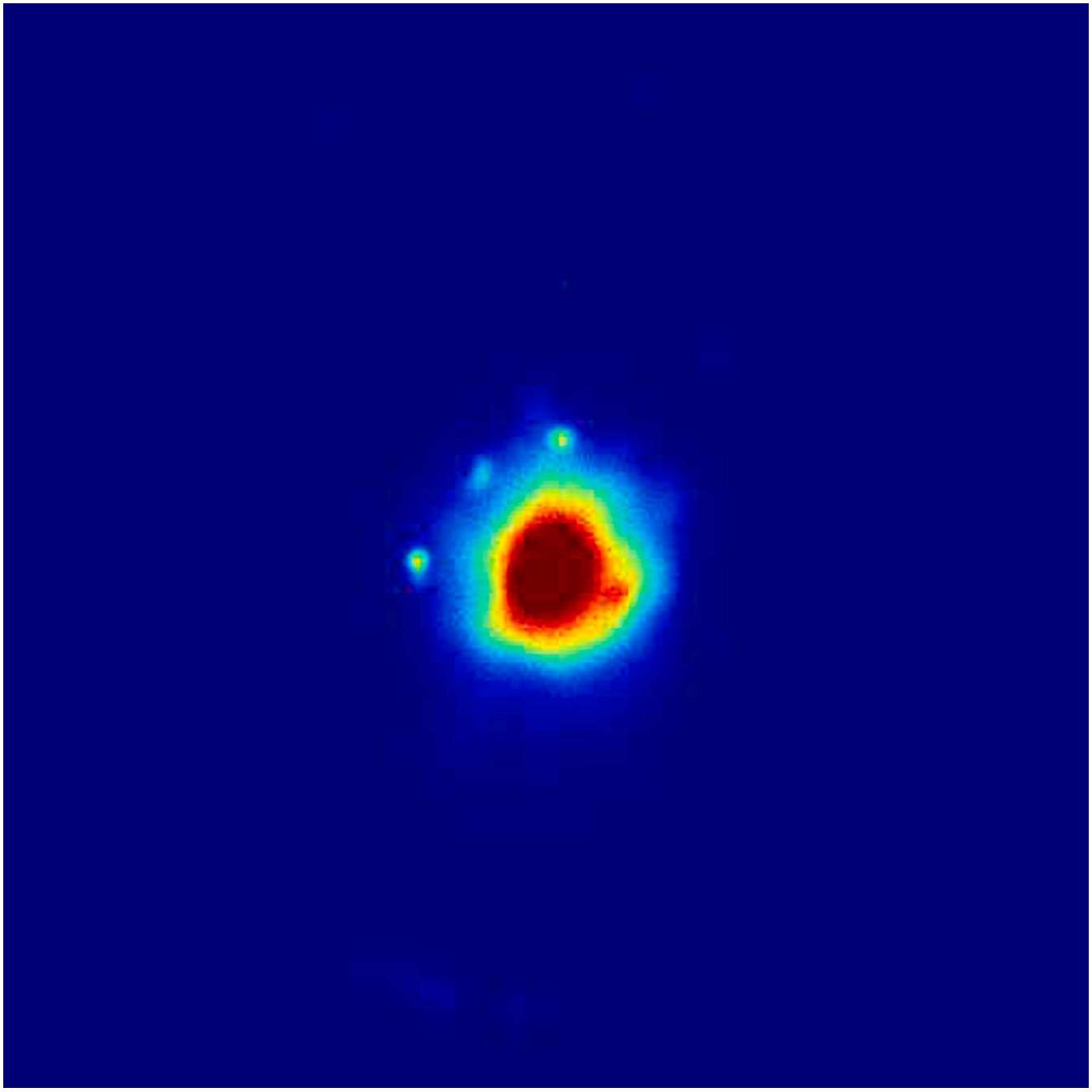

Video 13. A video clip is available online. Supplementary material related to this article can be found online at doi:10.1016/j.jmatprotec.2022.117823.

blocks were different, indicating that, for fixed build parameters, component geometry can significantly influence mechanical properties. In contrast, the means of the three 'With Control' blocks were not different, confirming that the control algorithm had successfully eliminated the effect of geometry on mechanical behaviour, improving mechanical homogeneity across different geometries and providing a robust baseline for future process improvement.

While this analysis has shown very promising results, there are a number of refinements which could be explored in future work. Incorporating a laser profilometer adjacent to the deposition nozzle would allow the physical width to be measured at a frequency comparable with the image capture, and therefore refine the calibration between image width and physical width. The power modulation calculation is very basic and while the control algorithm corrected the component-scale trends, there was no improvement in the low-level noise. A more complex modulation calculation could provide control over this low-level noise, achieve control more quickly, and yield a further reduction in mechanical property variation.

- Used fixed build parameters, component geometry was observed to affect melt pool width and resulting bulk mechanical properties in multi-hatch, multi-layer blocks built from 316 L by directed energy deposition
- Thin walled structures showed an increase in melt pool width with build height while the multi-hatch, multi-layer blocks showed a decrease, indicating a further geometry influence in the balance between different heat loss mechanisms

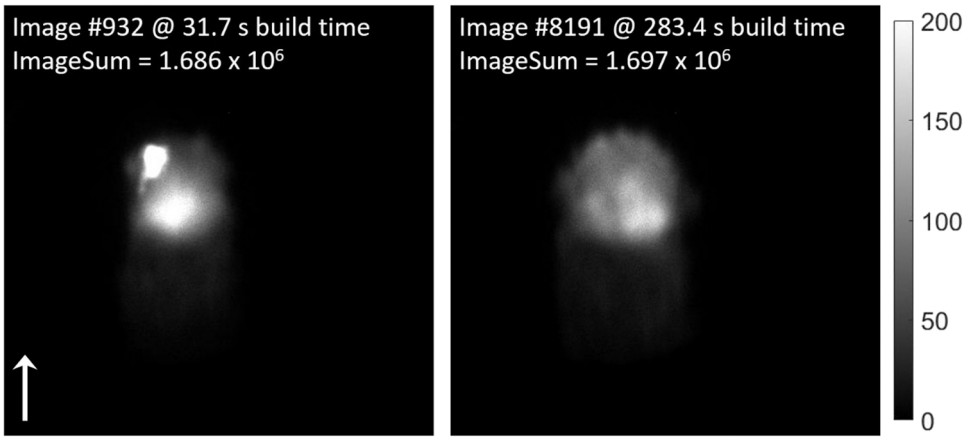

Fig. 5. Images from cylinder built at 250 W, 2200 mm/s, Repeat #1. Two images with comparable ImageSum but different melt pool size and intensity. Arrow shows laser travel direction. Images show the 0–200 section of the intensity range.

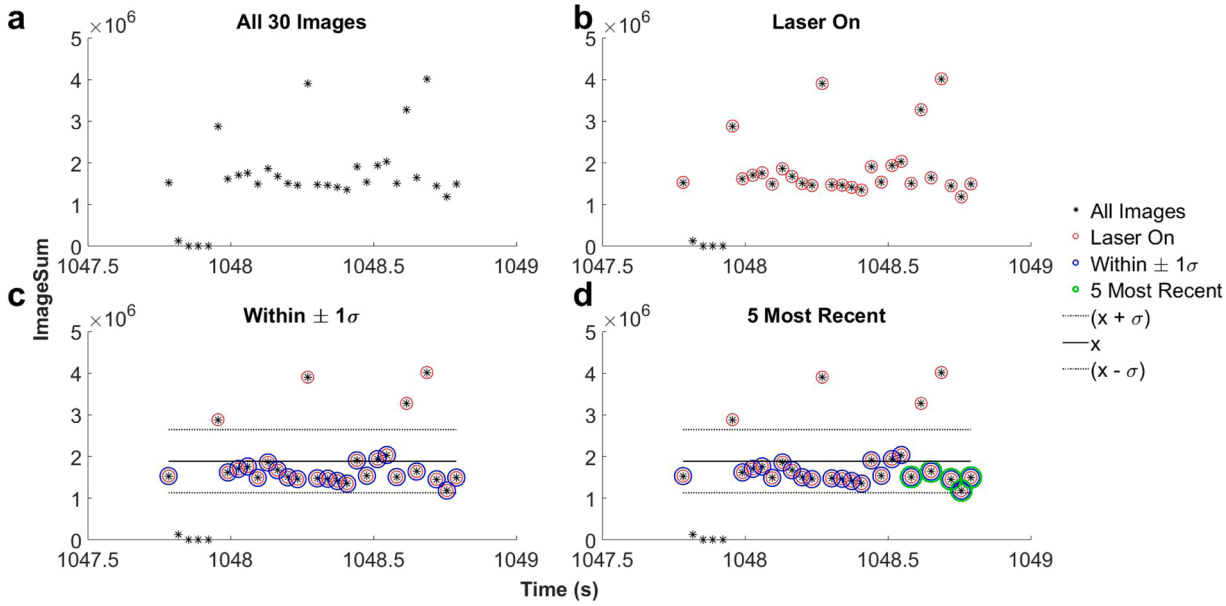

Fig. 6. Graphical demonstration of filtering approach, using 30 images from the Square block build. a) All 30 images brought into one control loop; b) Selection of images where the laser is on; c) Selection of images within 1 standard deviation of the mean; d) Selection of the most recent 5 images.

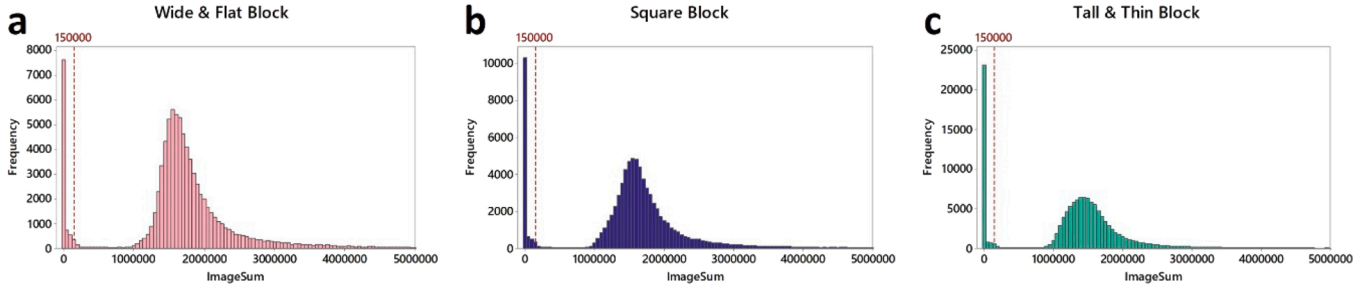

Fig. 7. Histograms of ImageSum for the three blocks, with the fixed threshold at 1.5 × 10^5 identified. Difference in y-axis scale highlights the difference in time spent with the laser off (ImageSum <1.5 ×10^5) for the different geometries.

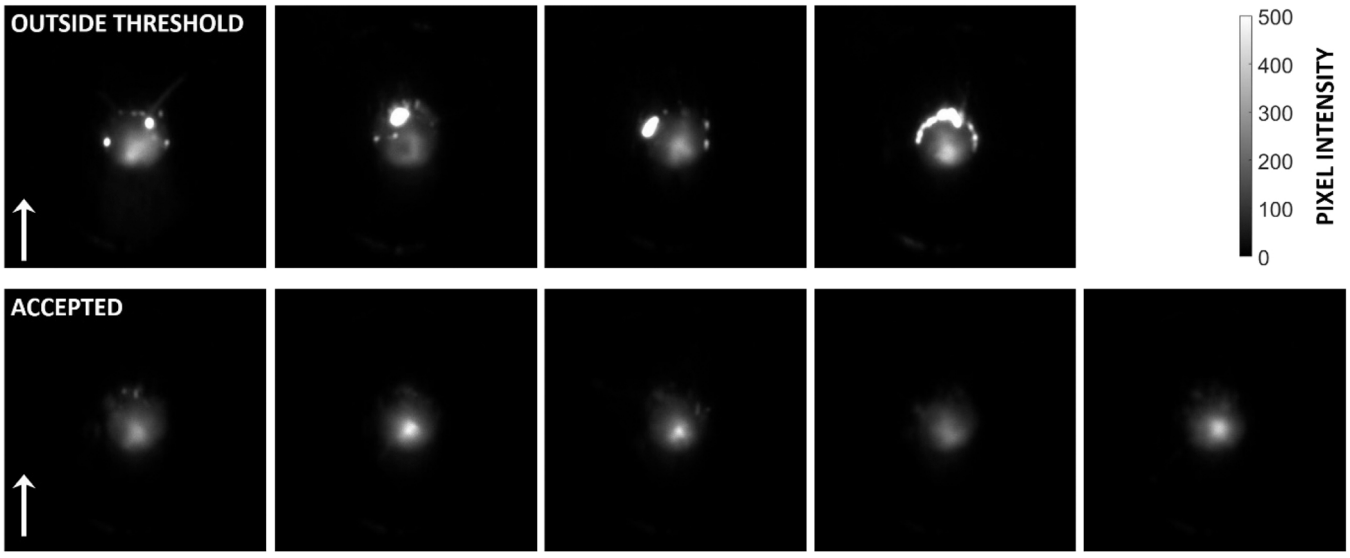

Fig. 8. Top row: Images from Fig. 6 which were rejected for being outside the selection threshold; Bottom row: Images from Fig. 6 which are acceptable to be used for width measurement.

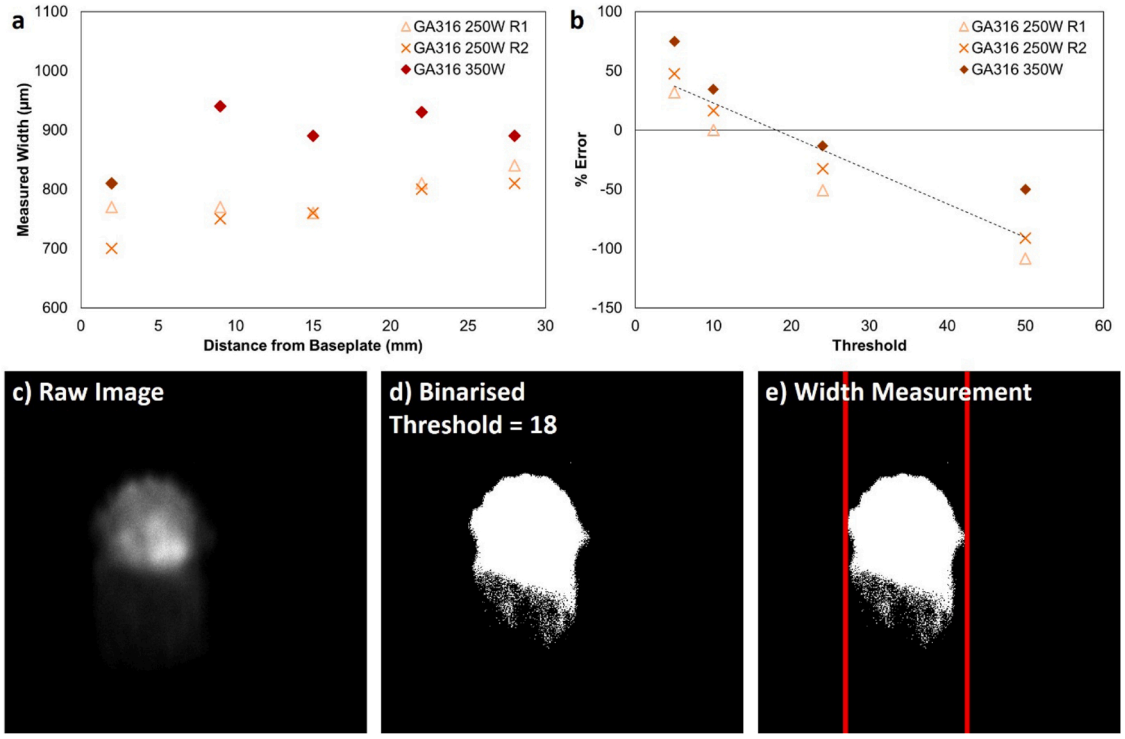

Fig. 9. a) Measured width of single hatch cylinders as a function of height; b) Calibration of greyscale threshold for identifying melt pool edge, aiming to minimise error between physical measurement of single hatch wall width and image measurement of melt pool width across all three cylinder builds; c)-e) Sequence of binarising and extracting width measurement from an image.

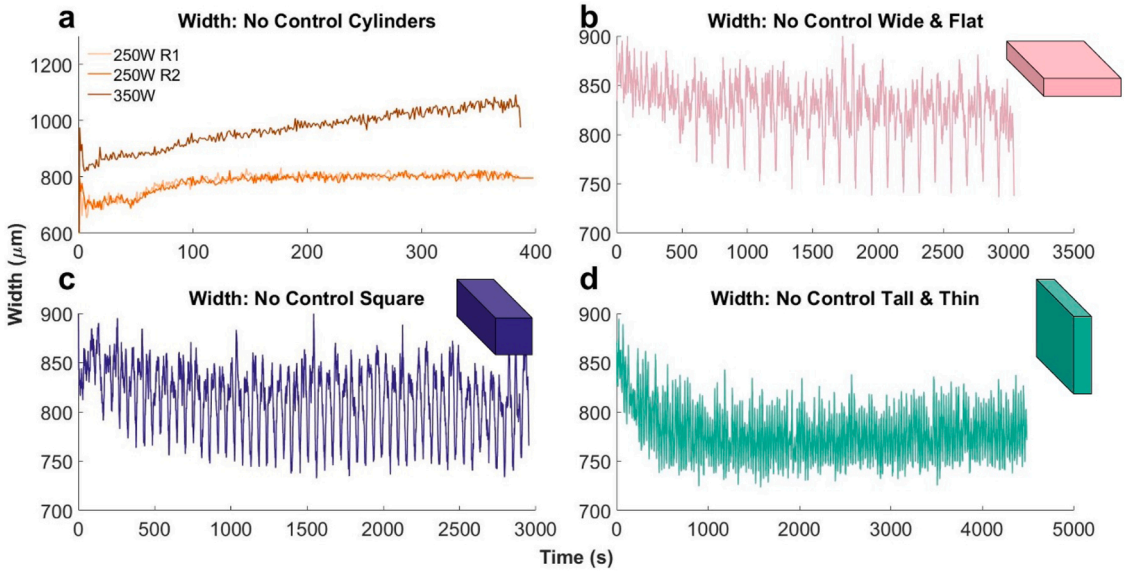

Fig. 10. Width for GA316 cylinders and blocks built 'No Control'. a) All three cylinders combined; b) Wide & Flat block with 80 hatches and 25 layers; c) Square section block with 34 hatches and 55 layers; d) Tall & Thin block with 16 hatches and 165 layers. Cylinder data displayed as moving average over 30 images (≈1 s), block data displayed as moving average over 300 images (≈10 s).

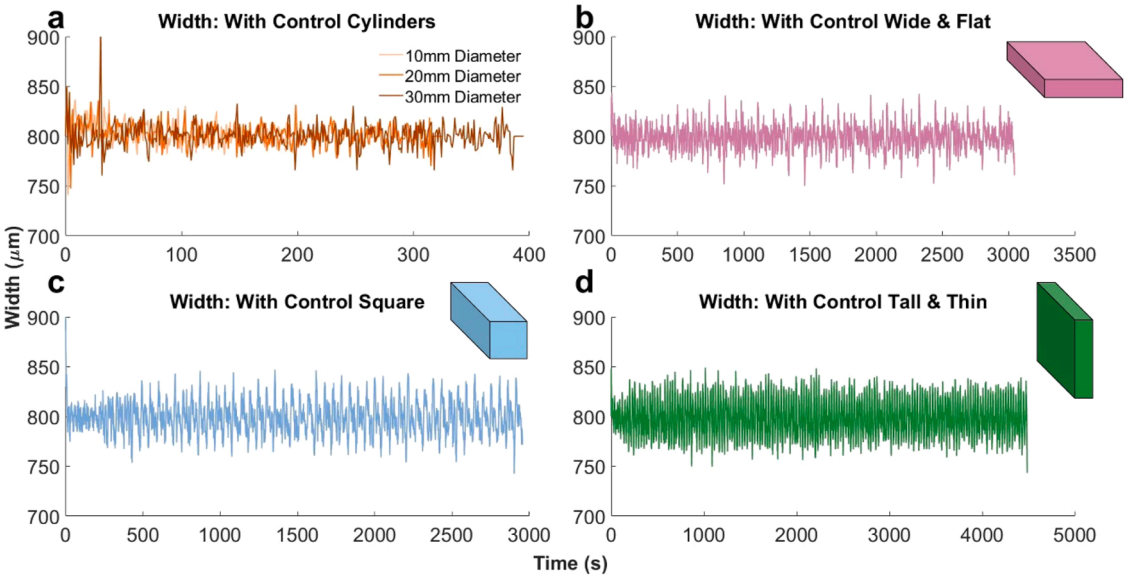

Fig. 11. Width for GA316 cylinders and blocks built 'With Control'. a) All three cylinders combined; b) Wide & Flat block with 80 hatches and 25 layers; c) Square section block with 34 hatches and 55 layers; d) Tall & Thin block with 16 hatches and 165 layers. Cylinder data displayed as moving average over 30 images (≈1 s), block data displayed as moving average over 300 images (≈10 s).

Table 1
Summary data for each build, by geometry and control type. Final power and mean width are calculated from the second half of each build, to exclude baseplate effects. Error shown is 1 standard deviation.

Geometry	Control Type	Speed mm/s	Initial Power W	Final Power W	Mean Width μm
Block Wide & Flat	No Control	2200	270	N/A	829 ± 62
	With Control			262 ± 16	799 ± 60
Block Square	No Control			N/A	815 ± 65
	With Control			269 ± 21	799 ± 60
Block Tall & Thin	No Control			N/A	776 ± 58
	With Control			277 ± 19	799 ± 58
Cylinder 10 mm Φ	With Control	1400	250	174 ± 2	803 ± 13
Cylinder 20 mm Φ	With Control	1800	300	212 ± 2	802 ± 12
Cylinder 30 mm Φ	With Control	2200	300	246 ± 3	801 ± 13

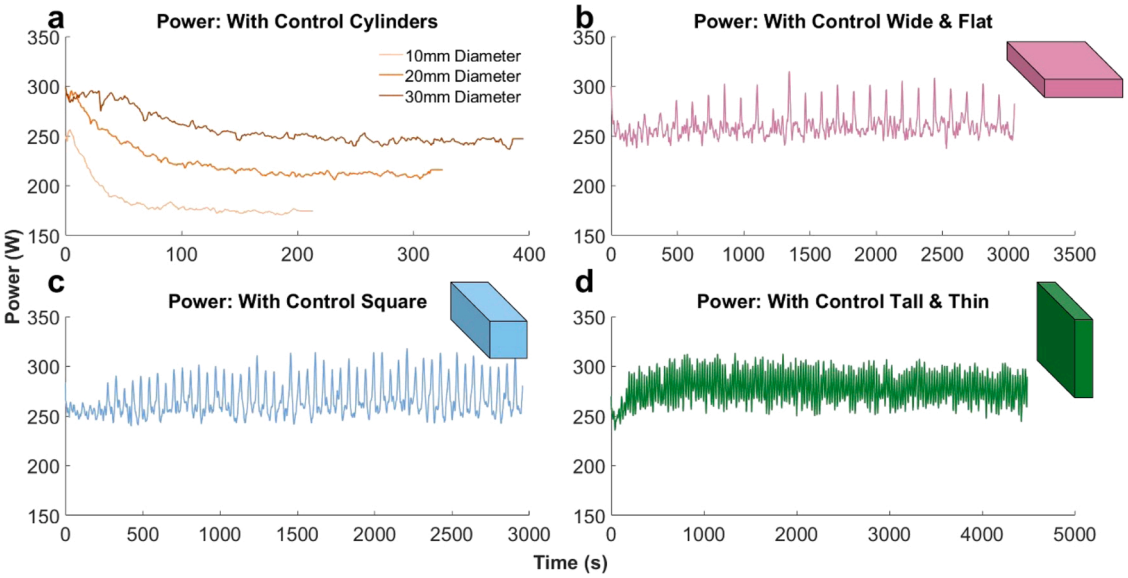

Fig. 12. Laser power for GA316 cylinders and blocks built 'With Control'. a) All three cylinders combined; b) Wide & Flat block with 80 hatches and 25 layers; c) Square section block with 34 hatches and 55 layers; d) Tall & Thin block with 16 hatches and 165 layers. Cylinder data displayed as moving average over 30 images (≈1 s), block data displayed as moving average over 300 images (≈10 s).

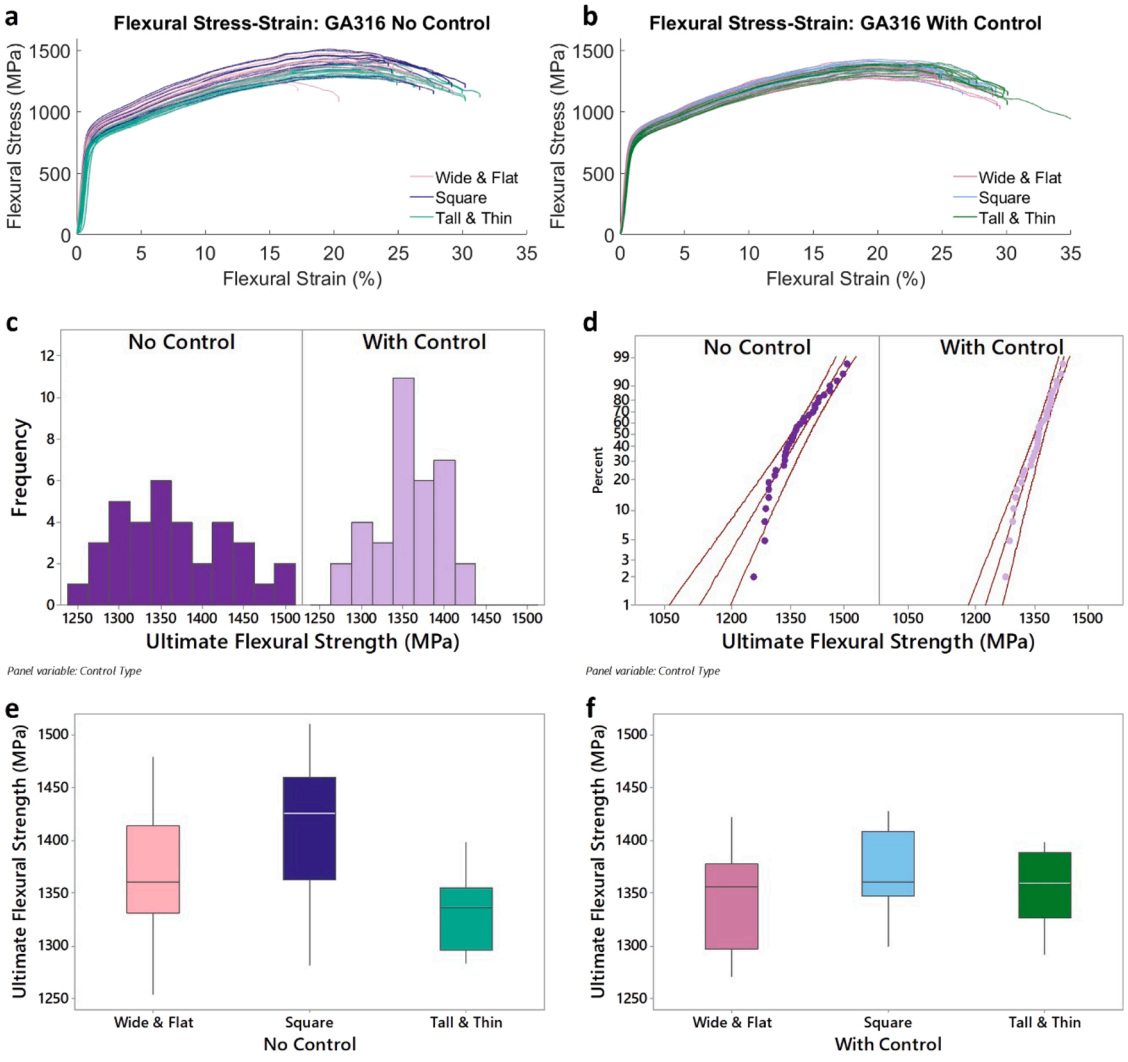

Fig. 13. 3-point bend test data for GA316 across three block geometries. a) Flexural stress-strain for 'No Control'; b) Flexural stress-strain for 'With Control'; c) Histograms and d) Weibull probability distributions for ultimate flexural strength for 'No Control' and 'With Control' with the three blocks geometries combined; e) and f) Boxplots for the individual block geometries.

- Closed-loop control of laser power produced a statistically significant reduction of the mechanical property distribution and eliminated the effects of component geometry and distance from the baseplate
- Statistical process control techniques were used to filter the live signal and extract representative images, successfully excluding those with spatter or where the laser is switched off
- The control approach, monitoring melt pool width using a low-cost coaxial camera running at a framerate of 30 Hz, was sufficiently robust to maintain an update frequency of 1 Hz over build durations of > 1 h

Funding

This work was funded by the Engineering and Physical Sciences Research Council through the Future Manufacturing Hub in Manufacture using Advanced Powder Processes (EP/P006566/1), and by the European Union's Horizon 2020 research and innovation programme under grant agreement No 820776, carried out under FoF-04–2018 project on the topic "Pilot lines on metal additive manufacturing" http://www.integraddeproject.eu/. We acknowledge the Henry Royce Institute for Advanced Materials, funded through EPSRC grants EP/R00661X/1, EP/S019367/1, EP/P02470X/1 and EP/P025285/1, for BeAM Magic 800 access at The University of Sheffield.

CRediT authorship contribution statement

F. Freeman: Conceptualization, Methodology, Software programming, Validation, Formal analysis, Investigation, Data curation, Writing – original draft preparation, Writing – review & editing, Visualization preparation, Project administration. **L. Chechik**: Software programming, Validation, Formal analysis, Data curation, Writing – review & editing. **B. Thomas**: Validation, Formal analysis, Data curation, Writing – review & editing. **I. Todd**: Resources, Writing – review & editing, Supervision, Funding acquisition.

Declaration of Competing Interest

The authors declare that they have no known competing financial interests or personal relationships that could have appeared to influence the work reported in this paper.

Data availability

Data will be made available on request.

Acknowledgements

The authors would like to thank Dr. Scott Notley for discussions on signal processing and noise reduction.

Appendix A. Supporting information

Supplementary data associated with this article can be found in the online version at doi:10.1016/j.jmatprotec.2022.117823.

References

Akbari, M., Kovacevic, R., 2019. Closed loop control of melt pool width in robotized laser powder–directed energy deposition process. Int J. Adv. Manuf. Technol. 104, 2887–2898. https://doi.org/10.1007/s00170-019-04195-y.

Bi, G., Gasser, A., Wissenbach, K., Drenker, A., Poprawe, R., 2006a. Characterization of the process control for the direct laser metallic powder deposition. Surf. Coat. Technol. 201, 2676–2683. https://doi.org/10.1016/j.surfcoat.2006.05.006.

Bi, G., Gasser, A., Wissenbach, K., Drenker, A., Poprawe, R., 2006b. Identification and qualification of temperature signal for monitoring and control in laser cladding. Opt. Lasers Eng. 44, 1348–1359. https://doi.org/10.1016/j.optlaseng.2006.01.009.

Blakey-Milner, B., Gradl, P., Snedden, G., Brooks, M., Pitot, J., Lopez, E., Leary, M., Berto, F., du Plessis, A., 2021. Metal additive manufacturing in aerospace: A review. Mater. Des. 209, 110008 https://doi.org/10.1016/j.matdes.2021.110008.

Catchpole-Smith, S., Aboulkhair, N., Parry, L., Tuck, C., Ashcroft, I.A., Clare, A., 2017. Fractal scan strategies for selective laser melting of "unweldable" nickel superalloys. Addit. Manuf. 15, 113–122. https://doi.org/10.1016/j.addma.2017.02.002.

Chechik, L., Boone, N.A., Stanger, L.R., Honniball, P., Freeman, F., Baxter, G., Willmott, J.R., Todd, I., 2020. Variation of texture anisotropy and hardness with build parameters and wall height in directed-energy-deposited 316L steel. Addit. Manuf. 38, 101806 https://doi.org/10.1016/j.addma.2020.101806.

Craeghs, T., Clijsters, S., Yasa, E., Bechmann, F., Berumen, S., Kruth, J.-P., 2011. Determination of geometrical factors in Layerwise Laser Melting using optical process monitoring. Opt. Lasers Eng. 49, 1440–1446. https://doi.org/10.1016/j.optlaseng.2011.06.016.

DebRoy, T., Wei, H.L., Zuback, J.S., Mukherjee, T., Elmer, J.W., Milewski, J.O., Beese, A. M., Wilson-Heid, A., De, A., Zhang, W., 2018. Additive manufacturing of metallic components – Process, structure and properties. Prog. Mater. Sci. 92, 112–224. https://doi.org/10.1016/j.pmatsci.2017.10.001.

Farshidianfar, M.H., Khodabakhshi, F., Khajepour, A., Gerlich, A.P., 2021. Closed-loop control of microstructure and mechanical properties in additive manufacturing by directed energy deposition. Mater. Sci. Eng.: A 803, 140483. https://doi.org/10.1016/j.msea.2020.140483.

Freeman, F.S.H.B., Thomas, B., Chechik, L., Todd, I., 2021. Multi-faceted monitoring of powder flow rate variability in directed energy deposition. Addit. Manuf. Lett. 10024. https://doi.org/10.1016/j.addlet.2021.100024.

Gibson, B.T., Bandari, Y.K., Richardson, B.S., Henry, W.C., Vetland, E.J., Sundermann, T. W., Love, L.J., 2020. Melt pool size control through multiple closed-loop modalities in laser-wire directed energy deposition of Ti-6Al-4V. Addit. Manuf. 32, 100993 https://doi.org/10.1016/j.addma.2019.100993.

Hofman, J.T., Pathiraj, B., van Dijk, J., de Lange, D.F., Meijer, J., 2012. A camera based feedback control strategy for the laser cladding process. J. Mater. Process. Technol. 212, 2455–2462. https://doi.org/10.1016/j.jmatprotec.2012.06.027.

Hu, D., Mei, H., Kovacevic, R., 2002. Improving solid freeform fabrication by laser-based additive manufacturing. Proc. Inst. Mech. Eng., Part B: J. Eng. Manuf. 216, 1253–1264. https://doi.org/10.1243/095440502760291808.

Kwon, O., Kim, H.G., Ham, M.J., Kim, W., Kim, G.H., Cho, J.H., Kim, N.I., Kim, K., 2020. A deep neural network for classification of melt-pool images in metal additive manufacturing. J. Intell. Manuf. 31, 375–386. https://doi.org/10.1007/s10845-018-1451-6.

Liao, S., Webster, S., Huang, D., Council, R., Ehmann, K., Cao, J., 2022. Simulation-guided variable laser power design for melt pool depth control in directed energy deposition. Addit. Manuf. 56, 102912 https://doi.org/10.1016/j.addma.2022.102912.

Mirazimzadeh, S.E., Pazireh, S., Urbanic, J., Hedrick, B., 2022. Investigation of effects of different moving heat source scanning patterns on thermo-mechanical behavior in direct energy deposition manufacturing. Int J. Adv. Manuf. Technol. 120, 4737–4753. https://doi.org/10.1007/s00170-022-08970-2.

Nassar, A.R., Keist, J.S., Reutzel, E.W., Spurgeon, T.J., 2015. Intra-layer closed-loop control of build plan during directed energy additive manufacturing of Ti–6Al–4V. Addit. Manuf. 6, 39–52. https://doi.org/10.1016/j.addma.2015.03.005.

Qi, H., Azer, M., Singh, P., 2010. Adaptive toolpath deposition method for laser net shape manufacturing and repair of turbine compressor airfoils. Int J. Adv. Manuf. Technol. 48, 121–131. https://doi.org/10.1007/s00170-009-2265-7.

Shrinivas Mahale, R., Shamanth, V., Hemanth, K., Nithin, S.K., Sharath, P.C., Shashanka, R., Patil, A., Shetty, D., 2022. Processes and applications of metal additive manufacturing. Materials Today: Proceedings, 5th International Conference on Advanced Research in Mechanical. Mater. Manuf. Eng. -2021 54, 228–233. https://doi.org/10.1016/j.matpr.2021.08.298.

Smoqi, Z., Bevans, B.D., Gaikwad, A., Craig, J., Abul-Haj, A., Roeder, B., Macy, B., Shield, J.E., Rao, P., 2022. Closed-loop control of meltpool temperature in directed energy deposition. Mater. Des. 215, 110508 https://doi.org/10.1016/j.matdes.2022.110508.

Stapenhurst, T., 2005. Mastering Statistical Process Control: A Handbook for Performance Improvement Using Cases. Taylor & Francis Group,, Jordan Hill, UNITED STATES.

Su, Y., Wang, Z., Xu, X., Luo, K., Lu, J., 2022. Effect of closed-loop controlled melt pool width on microstructure and tensile property for Fe-Ni-Cr alloy in directed energy deposition. J. Manuf. Process. 82, 708–721. https://doi.org/10.1016/j.jmapro.2022.08.049.

Tapia, G., Elwany, A., 2014. A review on process monitoring and control in metal-based additive manufacturing. J. Manuf. Sci. Eng. 136. https://doi.org/10.1115/1.4028540.

Thompson, S.M., Bian, L., Shamsaei, N., Yadollahi, A., 2015. An overview of Direct Laser Deposition for additive manufacturing; Part I: Transport phenomena, modeling and diagnostics. Addit. Manuf. 8, 36–62. https://doi.org/10.1016/j.addma.2015.07.001.

Yadollahi, A., Shamsaei, N., Thompson, S.M., Seely, D.W., 2015. Effects of process time interval and heat treatment on the mechanical and microstructural properties of direct laser deposited 316L stainless steel. Mater. Sci. Eng. A 644, 171–183. https://doi.org/10.1016/j.msea.2015.07.056.

Yang, Z., Lu, Y., Yeung, H., Krishnamurty, S., 2019, Investigation of Deep Learning for Real-Time Melt Pool Classification in Additive Manufacturing, in: 2019 IEEE 15th International Conference on Automation Science and Engineering (CASE). pp. 640–647. https://doi.org/10.1109/COASE.2019.8843291.

Zhang, F., Yu, K., Zhang, K., Liu, Yanlei, Xu, K., Liu, Yufang, 2015. An emissivity measurement apparatus for near infrared spectrum. Infrared Phys. Technol. 73, 275–280. https://doi.org/10.1016/j.infrared.2015.10.001.